ACS NANO

www.acsnano.org

ARTICLE

Metal–Organic Frameworks Modified Organic Bulk Heterojunction Interfaces for Effective Nongenetic Neuromodulation

Kangkang Weng,[#] Wenjun Li,[#] Xinyu Cheng,[#] Yunyun Xing,[#] Xin Fu, Yinghan Wang, Huachun Wang, Xiaoli Tian, Yuqi Wang, Lizhu Li, Jun Yao,[*] Xing Sheng,[*] Jinghong Li,[*] and Hao Zhang[*]

Cite This: *ACS Nano* 2025, 19, 16813–16828

Read Online

ACCESS | Metrics & More | Article Recommendations | Supporting Information

ABSTRACT: **Photoactive organic semiconductors, such as bulk heterojunctions (BHJs) of donor–acceptor pairs, are promising for building flexible devices for nongenetic and precise optical neuromodulation. However, the full potential of the diverse compositions and functionalities of BHJs has yet to be explored for neuromodulation due to their unsatisfactory interfaces with soft biotissues, which hinder signal transduction, tissue adhesion, and biocompatibility. Here, we address these challenges by introducing an interfacial layer composed of conductive and porous metal–organic frameworks (MOFs). The MOFs layer enhances charge injection capacity at the interface by >400 times and ensures tight and biocompatible junction between BHJs and biological materials. These improvements enable efficient electrical-to-ionic signal transduction for various BHJs, supporting reliable nongenetic modulation of cultured mouse hippocampal neurons under deep-red and near-infrared light. Moreover, flexible devices made from MOFs-modified BHJs allow for the *in vivo* stimulation of rat sciatic nerves at an ultralow light intensity threshold (0.01 mW mm^{-2}), 700 times lower than that required for unmodified devices. This interfacial engineering with porous MOFs can expand the material toolbox of BHJs-based photocapacitors and unlock more functionalities for neuromodulation and prosthetic biointerfaces.**

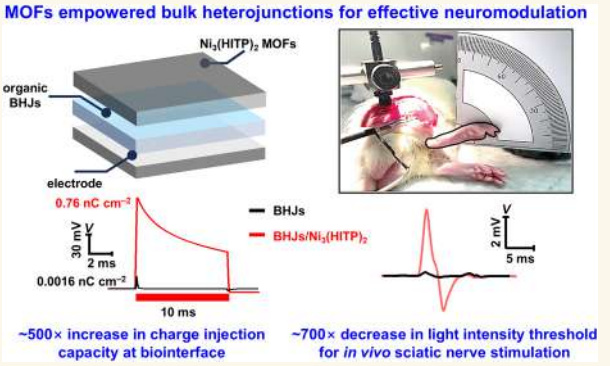

KEYWORDS: *neuromodulation, organic bulk heterojunctions, metal–organic frameworks, neural interfaces, photocapacitive effect*

INTRODUCTION

Precise and effective modulation of neuronal activity is essential for advancing both fundamental neuroscience research and clinical treatments of neurological disorders.[1−3] Recently, nongenetic optical neuromodulation using photoactive materials and devices interfaced with cells and biotissues has emerged as a promising approach.[4−7] Unlike traditional electrical stimulation with implantable electrodes[7,8] or optogenetics relying on light-sensitive opsins,[9] nongenetic neuromodulation offers spatiotemporal and multiscale control of neuronal activity—from the subcellular level to whole organisms[4,7,10]—without the need for wired connections or genetic modifications. Moreover, nongenetic optical neuromodulation leverages a wide range of functional materials, including the inorganic,[11−13] organic,[14,15] and nanoscale materials,[5,16] along with their diverse photocapacitive, photofaradaic (or photoelectrochemical), and photothermal processes.[17]

Organic photovoltaic materials, such as the BHJs of donor–acceptor blends[18−22] or the p/n junctions of small pigment molecules,[23,24] are representative systems for nongenetic optical neuromodulation. These materials possess low intrinsic stiffness, high light absorption coefficients, and excellent stability in biofluids, making them ideal for building ultrathin, flexible, and chronic implants for visual restoration[19,25,26] and peripheral nerve modulation.[27] These device features complement those of their inorganic counterparts, such as silicon, which often form bioresorbable, multiscale biointerfaces for neuromodulation via various mechanisms.[10,11,28,29] Moreover, the readily tunable compositions of organic photovoltaic materials, enabled by chemical synthesis and molecular engineering, offer great freedom in tailoring their material properties and device

Received: January 24, 2025
Revised: April 21, 2025
Accepted: April 21, 2025
Published: April 25, 2025

Downloaded via TSINGHUA UNIV on May 13, 2025 at 07:26:22 (UTC).
See https://pubs.acs.org/sharingguidelines for options on how to legitimately share published articles.

© 2025 American Chemical Society

https://doi.org/10.1021/acsnano.5c01516
ACS Nano 2025, 19, 16813–16828

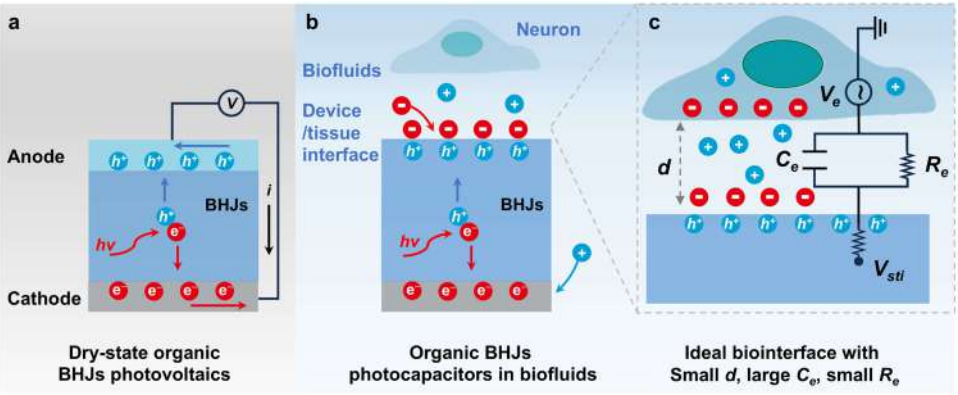

Figure 1. Comparison of the working principles of BHJs in photovoltaics and photocapacitive neuromodulation to highlight the importance of the biotic/abiotic interface. (a) In the dry-state photovoltaics, the device performance depends on the photogeneration of excitons and the separation of electrons and holes inside the BHJs layer. The separated charge carriers are collected at the electrodes to generate photovoltages or currents. (b) The photocapacitive neuromodulation relies on not only the generation and separation of electrical charges in the BHJs layer but also the formation of the electrolytic double layer and the ionic displacement currents at the biotic/abiotic interface. The charging and discharging of the photocapacitive double layer alter the membrane potential of neurons and modulate their activities. (c) A zoomed-in view of the biointerface and the equivalent circuits describing key parameters for the electrical-to-ionic signal transduction. An ideal interface between the BHJs photocapacitors (generating photoinduced stimulation voltage, V_{sti}) and neurons or biotissues (experiencing an electrical potential V_e) should ensure small separation distance (d), high double layer capacitance (C_e), and low resistance (R_e).

functionalities for various applications.[30−32] For instance, the molecular design of donor−acceptor pairs has led to an extensive library of BHJs with optimized spectral responses, improved charge separation kinetics, and enhanced material stability, which collectively drive the rapid progress in the field of organic photovoltaics.[33]

However, the impressive material versatility of organic BHJs, widely explored in photovoltaics, has rarely been exploited to advance their performance in neuromodulation. Most studies on neuromodulation with BHJs used a classic donor−acceptor pair, namely poly(3-hexylthiophene-2,5-diyl) (P3HT): [6,6]-phenyl-C61-butyric acid methyl ester (PCBM).[18] These P3HT:PCBM BHJs have led to successful demonstrations of photovoltaic retinal prostheses,[19,25,26] although the underlying stimulation mechanism remains unclear, potentially involving photocapacitive, photothermal, photoelectrochemical pathways or their combinations.[25,32] Despite these impressive results, it is notable that P3HT:PCBM are far from ideal photovoltaic BHJs, as they exhibit relatively low photoconversion efficiencies (PCEs, about 3%) and limited spectral range (below 650 nm, outside the tissue transparent window).[31,34] In contrast, BHJs with other compositions, such as those with nonfullerene acceptors, have shown enhanced PCEs (up to ≈20%) and extended spectral ranges exceeding 1000 nm. It is thus intuitive to expect that these high-performance photovoltaic BHJs could improve the efficiency in nongenetic optical neuromodulation and enable *in vivo*, deep-tissue applications.[24,31] However, reports on BHJs with compositions other than P3HT:PCBM (e.g., anilino squaraine (SQIB)[30,35] or benzothiadiazole-based donors (PCPDTBT) with PCBM acceptors[31] or p/n junctions with nonfullerene acceptors[32]) remain limited. These alternative BHJs have yet to show the anticipated improvements (compared to P3HT:PCBM) in neuromodulation performance.

The contrast in the performance of BHJs in photovoltaics and optical neuromodulation can be traced to their fundamentally different working principles.[19] The dry-state photovoltaics operate via the sequence of light absorption, exciton formation, and separation of the photogenerated electrical charges (Figure 1a), all occurring inside the polymer blends.[36] In comparison, photocapacitive neuromodulation in biofluids demands not only efficient electrical processes inside the BHJs but also the perturbation of ionic double layers at the device/electrolyte interfaces to modulate the membrane potential of neurons (Figure 1b).[6,14,11,23,35] These electrical-to-ionic signal transduction processes in BHJs-based neuromodulation rely on an additional set of parameters and require tailored designs at the biotic/abiotic interfaces.

In this work, we use a porous metal−organic frameworks (MOFs) interfacial layer to transform high-performance, nonfullerene photovoltaic BHJs into effective photocapacitors for neuromodulation. The conductive and two-dimensional (2D) Ni_3(2,3,6,7,10,11-hexaiminotriphenylene)$_2$ (or $Ni_3(HITP)_2$) MOFs layer, characterized by its high double-layer capacitance and low impedance, is an emerging electrochemical double layer material for supercapacitors.[25] Inspired by these properties, we utilized $Ni_3(HITP)_2$ MOFs to enhance the capacitive charge delivery at the biotic/abiotic interface for neuromodulation. When laminated onto the BHJs-based devices (e.g., PBDB-T donor with a nonfullerene ITIC acceptor, PCE ≈11% with a spectral range of 600−800 nm;[37] see full name of the donor−acceptor pairs in the Experimental Section), the MOFs layer increases the charge injection capacity of BHJs by more than 2 orders of magnitude (from 0.0016 to 0.76 nC cm^{-2}) and amplifies the photovoltages by 5 times (from ≈20 to ≈113 mV, irradiated by 635 nm light, 20 mW mm^{-2}, recorded in the electrolyte and relevant to neuromodulation). Compared to other types of interfacial materials previously reported (e.g., capacitive SiO_2 for SQIB:PCBM[35] and faradaic RuO_2[38,39] and PEDOT:PSS for P3HT:PCBM[40−42]), the $Ni_3(HITP)_2$ MOFs layer offers a significantly larger enhancement factor in charge injection capacity (≈470 versus <20 folds) and exhibits great material and device stability (over one month in biofluids-mimicking buffer solutions). Importantly, the stimulation of MOFs-modified BHJs relies solely on the double-layer photocapacitive mechanism, which avoids damage from redox reactions or heat, ensuring safe stimulation of cells or tissues. Additionally, the porous $Ni_3(HITP)_2$ MOFs layer enhances the adhesion of neurons to the BHJs layer, forming biocompatible

https://doi.org/10.1021/acsnano.5c01516
ACS Nano 2025, 19, 16813−16828

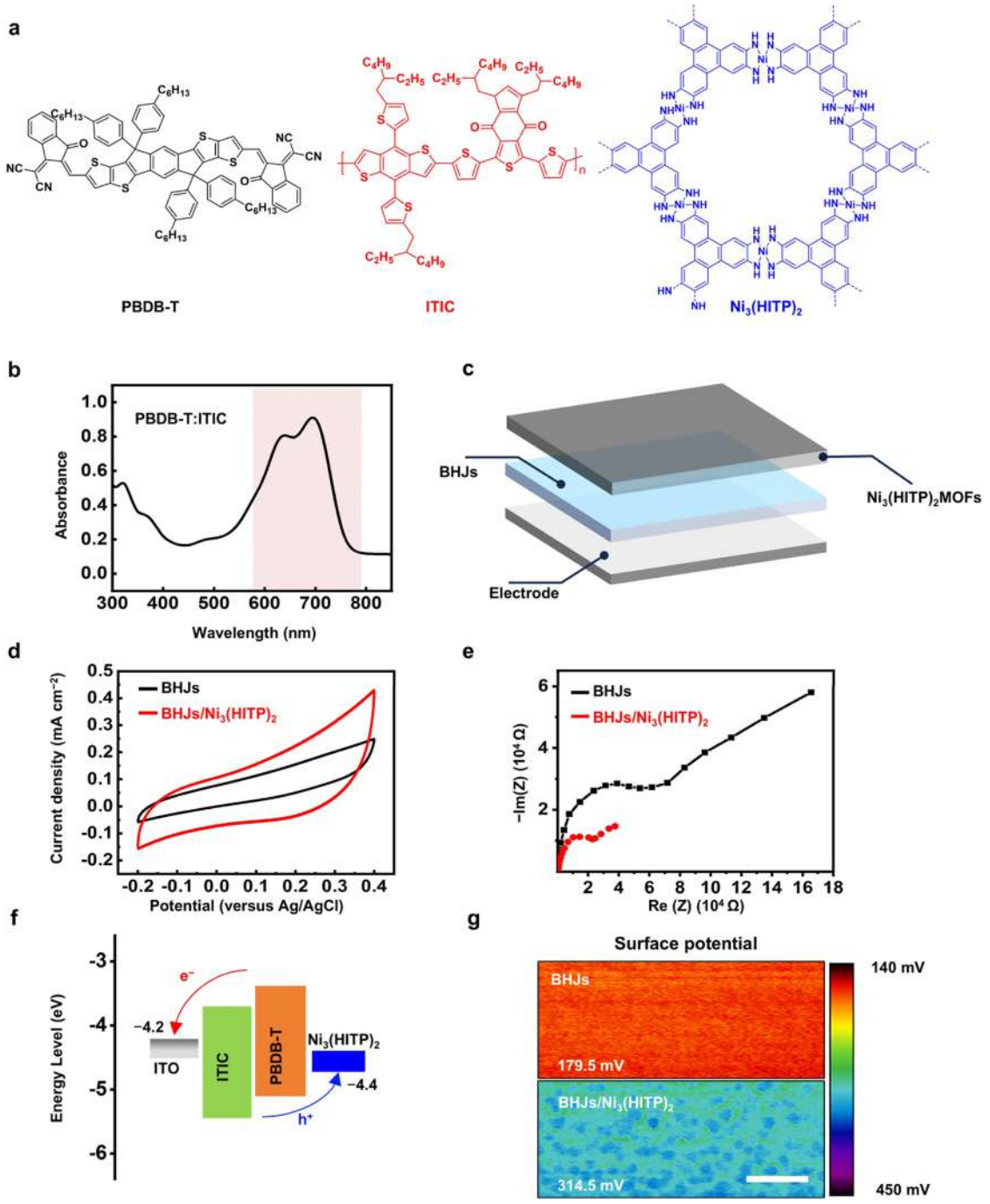

Figure 2. Design of the MOFs−modified BHJs photocapacitors. (a) Molecular structures of the organic donor (PBDB-T) and acceptor (ITIC) in the BHJs, and the $Ni_3(HITP)_2$ MOFs. (b) Absorption spectrum of the PBDB-T:ITIC BHJs (thickness, ≈100 nm). The red shaded area indicates the absorption of BHJs in deep red regions. (c) Schematic structure of the BHJs/$Ni_3(HITP)_2$ photocapacitors fabricated on conductive substrates. (d, e) Cyclic voltammetry (the 2nd scan, 100 mV s^{-1}) and electrochemical impedance spectra of BHJs−only and BHJs/$Ni_3(HITP)_2$ devices in PBS solution (0.01 M, pH = 7.4). (f) Energy level diagram of the BHJs/$Ni_3(HITP)_2$ devices. Holes are accumulated at the MOFs side, while electrons are collected at the ITO substrate. (g) Scanning KPFM image of BHJs−only and BHJs/$Ni_3(HITP)_2$ devices under 635 nm illumination (20 mW mm^{-2}). The latter show more positive surface charges. Scale bar, 1 μm.

and tight junctions. These features enable MOFs-modified BHJs to effectively modulate the activities and regulate the intercellular calcium dynamics of cultured neurons with single-cell resolution under 635 nm laser irradiation. Moreover, MOFs-modified BHJs fabricated in flexible formats demonstrate the ability to stimulate the rat sciatic nerves *in vivo* at an ultralow laser intensity threshold (about 0.01 mW/mm^2), which is 700 times lower than that required for unmodified BHJs. The strategy of using the $Ni_3(HITP)_2$ MOFs layer to electrically improve the biotic/abiotic interfaces is versatile for BHJs with different donor−acceptor pairs, including those with spectral coverage reaching 1000 nm. These results underscore the importance of interfacial design and highlight the potential of $Ni_3(HITP)_2$ MOFs and other interfacial materials to expand the scope and functionalities of BHJs-based nongenetic photocapacitive neuromodulation.

https://doi.org/10.1021/acsnano.5c01516
ACS Nano 2025, 19, 16813−16828

RESULTS AND DISCUSSION

Key Parameters for Effective Electrical-to-Ionic Transduction at Biointerfaces. The photocapacitive modulation of neuronal activity relies on the transduction of light-generated electrons in the devices into ion currents at the biotic/abiotic interface.[6,14] The process starts from the photogeneration and separation of charge carriers in the active semiconductor layer, e.g., BHJs (Figure 1b). Holes (or electrons) accumulate at the device/electrolyte interface, forming an oppositely charged double layer consisting of anions and cations. Meanwhile, electrons (or holes) are collected at the conductive back electrode and form an electrical double layer with the surrounding electrolytes.[23] The charging and discharging of the capacitive double layer at the interface then induce ionic displacement currents within the electrolyte, ultimately altering the membrane potential of neurons to facilitate up- and down-regulate their neuronal activity excitation or inhibition. These complex, interfacial electrochemical events can be modeled using a simplified equivalent circuit (Figure 1c). In this model, the transduction of the stimulation voltage (V_{sti}) generated by the device to the electrical potential (V_e) experienced by the cell membrane depends on several parameters at the interface, as described in eq 1.[17,43] These parameters include the width (d, the distance between device and biotissues) and the electrical properties of the interface. The latter can be represented as a parallel circuit of the leakage resistance R_e and the electrical double layer capacitance C_e in series with the interconnect resistance R_{ic}. Parameters σ and s in eq 1 are the electrical conductivity of the electrolyte and the complex frequency of interacting waveforms, respectively. According to eq 1, effective neuromodulation requires not only efficient photoelectric conversion inside the BHJs (shown in Figure 1a, the origin for high V_{sti}), but also the tight junction (small d) and favorable electrical properties (shown in Figure 1c, high C_e and low R_e) at the interface.

$$V_e = \frac{1}{4\pi\sigma d}\left[\left(\frac{1}{R_e} + sC_e\right)^{-1} + R_{ic}\right]^{-1} V_{sti} \quad (1)$$

Design of the MOFs-modified BHJs Devices. Our design of the MOFs-modified BHJs devices followed these requirements and used materials listed in Figure 2a. The photoactive organic BHJs layer contains poly[(2,6-(4,8-bis(5-(2-ethylhexyl)thiophen-2-yl)-benzo[1,2-b:4,5-b′]dithiophene))-*alt*-(5,5-(1′,3′-di-2-thienyl-5′,7′-bis(2-ethylhexyl) benzo[1′,2′-c:4′,5′-c′]dithiophene-4,8-dione))] (PBDB-T) as the donors and 3-((1,1-dicyanomethylene)-indanone)-5,5,11,11-tetrakis-(4-hexylphenyl)-dithieno[2,3-d:2′,3′-d′]-s-indaceno[1,2-b:5,6-b′]dithiophene (ITIC) as the acceptors. These donor−acceptor BHJs composites are representative nonfullerene based materials for constructing organic photovoltaics with high efficiency (or high V_{sti}) and long device lifetime.[44] Compared to P3HT:PCBM, PBDB-T:ITIC based photovoltaics show much higher optimal PCE (11% versus 3%) and extended photoresponsive spectral range (from 450−500 to 600−800 nm, Figure 2b). The absorption and photovoltaic characteristics of PBDB-T:ITIC in the deep-red light regime align with the tissue transparency window and favor their uses in implantable devices designed for deep-tissue neuromodulation.

The key to the design is using a 2D conductive MOFs layer between the BHJs device and biotissues. These MOFs, abbreviated as $Ni_3(HITP)_2$, are composed of Ni^{2+} cations and HITP linkers. $Ni_3(HITP)_2$ MOFs feature stacked 2D π-conjugated layers interspersed with one-dimensional (1D) cylindrical channels of 1.5 nm in diameter.[45] The choice of $Ni_3(HITP)_2$ MOFs as the interfacial layer follows the following considerations. First, the structures offer $Ni_3(HITP)_2$ a unique combination of high porosity, large surface area (~630 $m^2\ g^{-1}$), excellent electrical conductivity (5000 S m^{-1}), and high areal capacitance (18 μF cm^{-2}),[45] which helps improving the signal transduction efficiency at the interface. Second, $Ni_3(HITP)_2$ MOFs possess suitable energy levels for a built-in electric field that promote charge separation within the device. Third, the 2D $Ni_3(HITP)_2$ layer can readily form at the air−liquid interface and be transfer-printed atop the BHJs layers without degrading their structural integrity. These merits render $Ni_3(HITP)_2$ an ideal interfacial layer, enabling tight junction between the BHJs device and biotissues and improved electrical properties at the interface.

We then built MOFs-modified BHJs devices to elaborate the effects of the $Ni_3(HITP)_2$ layer on the interfacial properties. Device fabrication starts from spin-coating the BHJs layer (100 nm, PBDB-T/ITIC = 1:1 in mass) on indium tin oxide (ITO)-coated glass (Figure 2c), followed by the stamp transfer-printing of a uniform $Ni_3(HITP)_2$ layer (30 nm) atop the BHJs (Figure S1). The integration between $Ni_3(HITP)_2$ and BHJs layers did not require additional surface treatments. The strong $\pi-\pi$ interaction between $Ni_3(HITP)_2$ and BHJs layers ensures their seamless integration without the need of additional surface treatments. For comparison, we also prepared devices without the $Ni_3(HITP)_2$ layer, referred to as BHJs-only devices. The increased integral area (e.g., from 0.3 to 1.65 mF cm^{-2} for data collected at scan speed of 100 mV s^{-1}) of the cyclic voltammetry data of BHJs/$Ni_3(HITP)_2$ device in Figures 2d and S4 reflects an increased electrical double layer capacitance C_e. In parallel, the large surface area and porous structures of the $Ni_3(HITP)_2$ layer facilitate ion transfer and charge storage, resulting in a reduced interfacial impedance R_e,[14,46] by a factor of ≈3 (Figure 2e). Additionally, the introduction of the optically transparent $Ni_3(HITP)_2$ (Figure S2) is also beneficial to the photoelectric conversion of BHJs. The built-in electric field between $Ni_3(HITP)_2$ (work function ≈4.4 eV, Figure S3) and ITO (work function ≈4.2 eV) (Figure 2f) may potentially promote charge separation across the BHJs layer and increase V_{sti}. Upon illumination with a 635 nm laser (20 mW mm^{-2}), excitons in the BHJs layer readily dissociate. Electrons are injected into ITO electrode, while holes accumulate at the interface between $Ni_3(HITP)_2$ layer and electrolyte. This leads to a more positive surface potential in the MOFs-modified BHJs device (Figure 2g, 314.5 mV, versus 179.5 mV for the BHJs-only device), as measured by the Kelvin probe force microscopy (KPFM). It is worth noting that the KPFM images were collected from dry-state, illuminated devices. While the absolute surface potential data may differ from those for devices immersed in biofluids and convey limited quantitative information, the observed trend strongly supports that the photoinduced potential of BHJs/$Ni_3(HITP)_2$ devices is higher than that of their BHJs-only counterpart.

Amplified Photovoltage at the Interface by Introducing the MOFs Layer. The desirable changes in C_e, R_e, and V_{sti} in $Ni_3(HITP)_2$ modified devices sets the foundation for effective electrical-to-ionic transduction at the biotic/abiotic interface. To validate this, we measured the photovoltage generated by devices in an electrolyte (phosphate-buffered saline, or PBS, pH = 7.4) using a glass micropipette electrode (Figure 3a). The

https://doi.org/10.1021/acsnano.5c01516
ACS Nano 2025, 19, 16813−16828

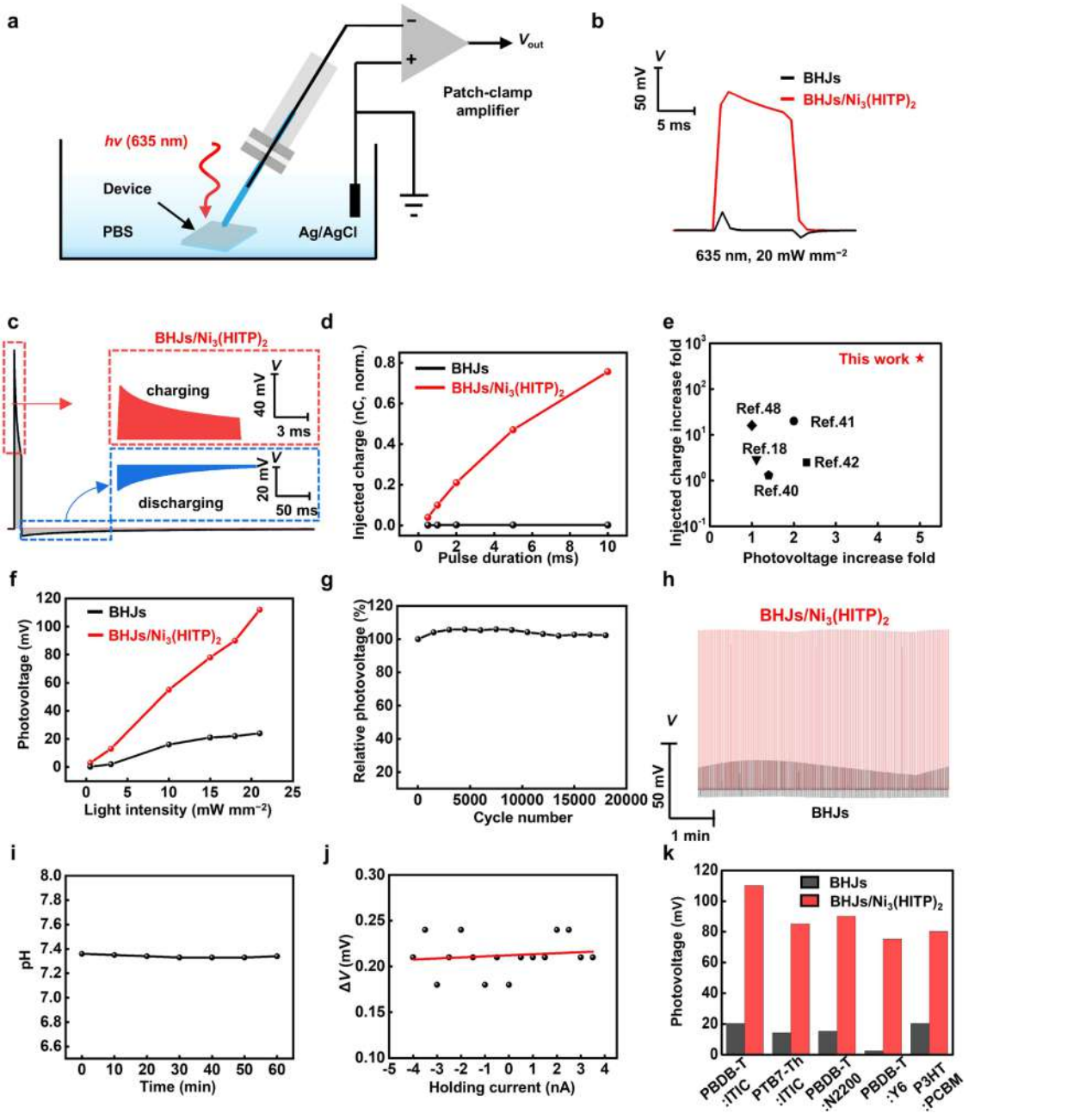

Figure 3. Amplified photocapacitive responses of BHJs/$Ni_3(HITP)_2$ device. (a) Scheme of the patch-clamp setup used to measure the photoresponses/photoinduced voltages of devices. A 635 nm laser (spot size, ≈4 mm; light intensity, 20 mW mm^{-2}) was used for collecting data shown in all subsequent panels. (b) Photovoltage traces recorded from BHJs-only and BHJs/$Ni_3(HITP)_2$ devices. Pulse duration, 1 ms. (c) Representative photovoltage curves highlighting the charging and discharging phases. Pulse duration, 10 ms. Inset shows the magnified view of charging and discharging phases. (d) The amount of injected charges extracted from the photocurrent measurements of 635 nm illuminated BHJ-only and BHJ/$Ni_3(HITP)_2$ devices as the function of pulse duration. (e) Comparison of the enhancement fold in injected charge levels and photovoltages of devices with or without the interfacial layer. Data from this work (interfacial layer, $Ni_3(HITP)_2$) and previous reports (using metal oxides or PEDOT:PSS interfacial layers) were collected with a pulse duration of 10 ms. (f) Photovoltage generated by devices at various light intensities. (g) Relative changes in photovoltage of BHJs/$Ni_3(HITP)_2$ devices during repetitive illumination cycles (frequency, 5 Hz; pulse width, 1 ms). (h) Comparison of the photovoltage changes of BHJs-only (black traces) and BHJs/$Ni_3(HITP)_2$ (red traces) devices during repetitive illumination. (i) Monitoring of pH changes in extracellular solution (initial pH, 7.4) upon continuous light illumination (60 min) of the immersed BHJs/$Ni_3(HITP)_2$ device. (j) The $\Delta V_{light,1\ ms}$ versus I_0 plot shows a negligible slope and an intercept of ≈0.20 mV, indicating minimal photothermal responses. (k) Amplification of photovoltage of different BHJs devices, by about 5-fold, after the introduction of $Ni_3(HITP)_2$ interfacial layers.

patch pipette was positioned approximately 10 μm above the device surface and measured photovoltage versus a floating Ag/AgCl electrode induced by an incident red laser (635 nm, spot size, ≈4 mm). Results from this measurement reflect the operational condition of a freestanding implantable device in the biological environment and serve as a surrogate for the electrical perturbation experienced by biological tissues during neuromodulation.[24,28] Figure 3b compares the typical photovoltage of

https://doi.org/10.1021/acsnano.5c01516
ACS Nano 2025, 19, 16813−16828

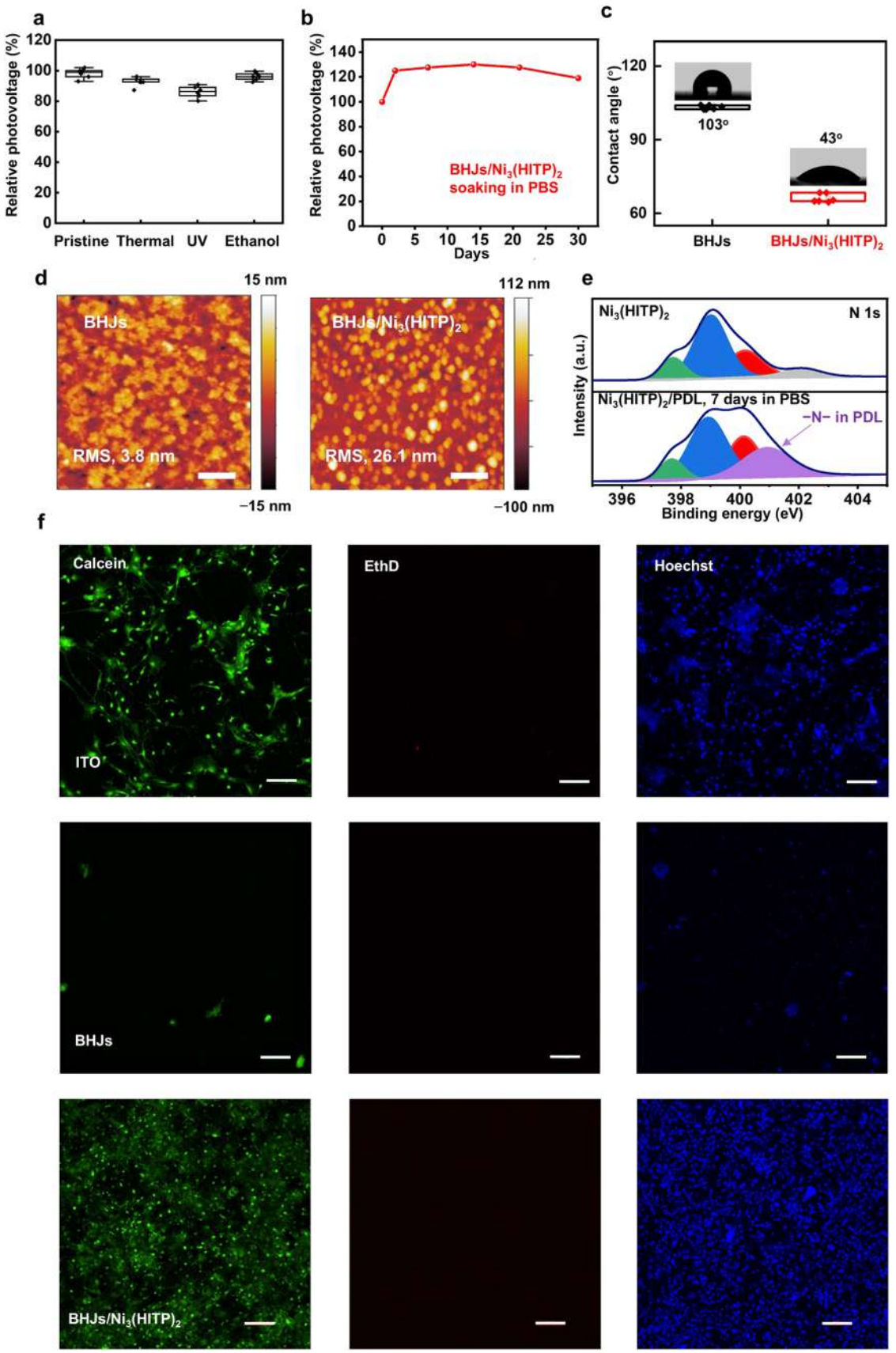

Figure 4. Stable and biocompatible interfaces between cultured hippocampal neurons and BHJs/$Ni_3(HITP)_2$ devices. (a) Retention of photovoltage of BHJs/$Ni_3(HITP)_2$ devices after various sterilization processes. A total of six measurements ($n = 6$) were conducted. The box plots show the interquartile range (IQR) centered around the median, with whiskers extending to 1.5 times the IQR above and below the box. (b) Retention of photovoltage of BHJs/$Ni_3(HITP)_2$ devices after soaking in PBS solution for a month. (c) Contact angles of BHJs-only and

https://doi.org/10.1021/acsnano.5c01516
ACS Nano 2025, 19, 16813−16828

Figure 4. continued

BHJs/$Ni_3(HITP)_2$ films. Box plots represent the IQR divided by the median with whiskers extending up to 1.5 times the IQR. Each box was calculated from at least three different locations on two separate samples ($n \geq 6$). (d) AFM images showing the surface roughness of BHJs-only and BHJs/$Ni_3(HITP)_2$ devices. (e) XPS data of (top) $Ni_3(HITP)_2$ and (bottom) PDL-coated $Ni_3(HITP)_2$ films. The N 1s signals from PDL layer remained after soaking the PDL-coated $Ni_3(HITP)_2$ films in water for 7 days. (f) Immunofluorescence images of mouse primary hippocampal neurons cultured on the ITO (control), BHJs, and BHJs/$Ni_3(HITP)_2$ films using the live/dead assay. The images with blue (Hoechst), green (Calcein AM), and red (Ethidium homodimer-1, EthD-1) color represent cell nuclei, live cells, and dead cells, respectively. Scale bars, (d) 1 μm, (f) 100 μm.

BHJs-only and BHJs/$Ni_3(HITP)_2$ devices under mild irradiation (20 mW mm^{-2}). According to the device polarity (Figure 3c), illumination leads to hole accumulation at the interface, which subsequently causes a cathodic transient photovoltage peak for charging followed by a slow, second peak for discharging. The nearly identical integrated areas of both peaks suggest charge-balanced biphasic stimulation with negligible faradaic processes. The transient, photocapacitive modulation mechanism, arising from the electrochemical double layer behavior of $Ni_3(HITP)_2$, is desirable as they avoid the damage of tissues or devices and prevent the generation of toxic byproducts.[14] Compared to BHJs-only devices, the BHJs/$Ni_3(HITP)_2$ devices show a 5-fold increase in photovoltage (from 20 to 113 mV, Figure 3b) and ≈100-fold increase in the charge injection density (from 0.001 to 0.1 nC cm^{-2}, Figure 3d), when illuminated with a short-pulsed laser (duration ≈1 ms). With prolonged irradiation (10 ms duration), the charge injection density reaches 0.76 nC cm^{-2}, representing a ≈470-fold increase compared to BHJs-only devices (Figures 3d and S5a). Such substantial amplifications in photovoltage and charge injection efficiency compare favorably with enhancements introduced by dielectric,[47] metallic,[26] and pseudocapacitive (PEDOT:PSS[40,48] or RuO_2[38]) coatings on organic optoelectronic devices for neuromodulation, as summarized in Figure 3e. Figure 3f shows the dependence of photovoltage on light intensity for BHJs-only and BHJs/$Ni_3(HITP)_2$ devices. As light intensity increases from 0.5 to 20 mW mm^{-2}, photovoltage of BHJs/$Ni_3(HITP)_2$ devices increases from 3 to 113 mV, compared to 0.2 to 24 mV for the BHJs-only counterparts. The stronger dependence of photovoltage on light intensity in BHJs/$Ni_3(HITP)_2$ devices follows from the suppressed charge recombination. Additionally, we measured photovoltages of BHJs-only and BHJs/$Ni_3(HITP)_2$ devices under illumination by light of various wavelengths (470, 635, and 808 nm). As shown in Figure S6, the trend in the photovoltages aligns with the absorption spectrum of PBDB-T:ITIC. In all cases, the BHJs/$Ni_3(HITP)_2$ devices show improved performance than the BHJs-only counterpart.

The BHJs/$Ni_3(HITP)_2$ devices show decent operational stability. When illuminated at an irradiance of 20 mW mm^{-2} (pulse frequency, 5 Hz; duration, 1 ms), these devices show almost unaltered photovoltage after over 18,000 cycles (Figure 3g,h). They also remain stable at higher operational frequencies (10 Hz, Figure S5b). In contrast, BHJs-only devices show fluctuating photovoltage even during short-term operation (Figure 3h), presumably due to charge-induced changes in the surface energy of BHJs materials. We tend to attribute the improved operational stability of BHJs/$Ni_3(HITP)_2$ devices to the low R_e, which favors fast charging/discharging processes. This is supported by the rapid rise (≈86 μs)/decay (≈160 μs) in the photovoltage changes (Figure S5c), which prevents prolonged charge accumulation and mitigates device degradation.

We further assessed the potential pathways of BHJs/$Ni_3(HITP)_2$ devices in neuromodulation. The measured photocurrents (Figure S7) show a negligible fraction of faradaic component (≈1.5% to the peak capacitive current). Additionally, no changes in the pH of the electrolyte were observed during device operation under continuous illumination for 1 h (Figure 3i). These results exclude the possibility of photofaradaic processes during neuromodulation, which could disrupt the homeostasis of the cellular environment and compromise device stability. Photothermal effect represents another potential pathway by which organic BHJs can alter the membrane potential.[22] We monitored the temperature changes indirectly from the photovoltage curve (Figure 3j), following the method described in ref 8. The linear regression analysis reveals a weak correlation between the holding current and recorded photovoltages, indicating minimal photothermal currents in our measurements. Collectively, these results confirm that the amplification of photovoltage by the interfacial $Ni_3(HITP)_2$ layer solely arises from the photocapacitive pathway, which ensures safe and reliable extracellular neuromodulation.

Moreover, the amplification of photovoltage by the interfacial $Ni_3(HITP)_2$ layer is general to BHJs with various donor−acceptor combinations. About 5-fold increases in the photovoltages (Figure 3k) were observed when the MOFs layer was added to various BHJs materials (Figure S8, see full names of the donors and acceptors in Experimental Section). A similar trend was also observed in the case of P3HT:PCBM with or without the MOFs layer (Figure 3k). The versatility of this approach expands the material toolbox for organic optoelectronic biointerfaces, which may enable the construction of devices with higher efficiencies, better compatibility, and extended spectral responses. For example, BHJs with Y6 acceptor have strong absorption in the near-infrared regime (700−1000 nm) and thus possess great potential for neuromodulation with light of longer wavelengths, which cannot be achieved by conventional P3HT:PCBM based devices.[31] Under near-infrared light (808 nm), the MOFs-modified PBDB-T:Y6 BHJs show an increase in photovoltage from 5 to 75 mV.

Stable, Tight, and Biocompatible Interface between Neurons and MOFs-modified Devices. Chronic implants for neuromodulation also require stable, mechanically compliant, and biochemically inert junction at the biotic/abiotic interfaces. The presented BHJs/$Ni_3(HITP)_2$ devices meet all these requirements. The devices are compatible with typical sterilization procedures, including germicidal ultraviolet (UV) exposure, rinsing with 70% ethanol, or thermal treatment (150 °C, 30 min). Poststerilization, the reduction in photovoltage is 2−6% for ethanol and thermally treated devices, and slightly higher (≈12%) for UV exposed ones (Figure 4a). Importantly, the photovoltage of sterilized devices remains sufficient for effective optical neuromodulation. Moreover, the BHJs/$Ni_3(HITP)_2$ devices retain their original photovoltage after being immersed in a PBS solution for over one month, which

https://doi.org/10.1021/acsnano.5c01516
ACS Nano 2025, 19, 16813−16828

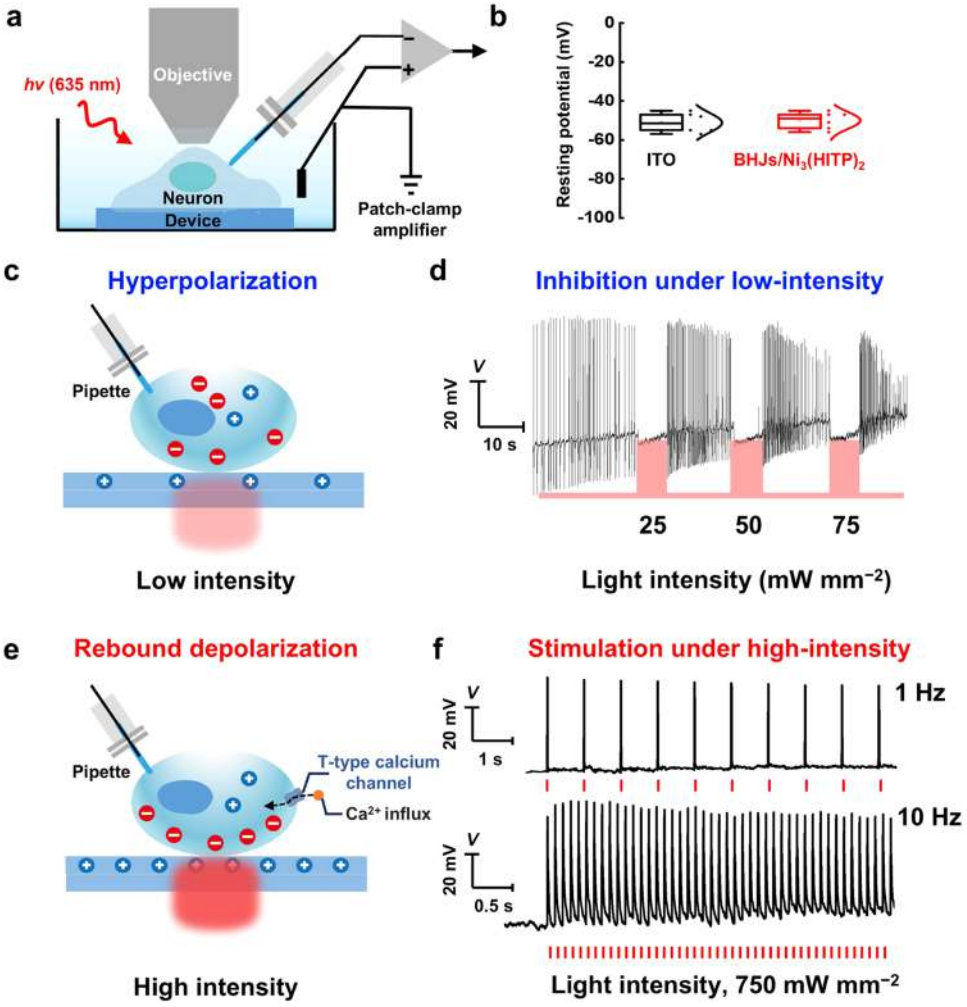

Figure 5. ***In vitro*** **optoelectronic modulation of neuronal activity with BHJs/$Ni_3(HITP)_2$ devices. (a) Schematic illustration of the setup for optical neuromodulation of cultured rat DRG neurons and recording of the membrane potential. A 635 nm laser with a spot size of ≈500 μm was used. (b) Recorded resting membrane potential of cultured rat DRG neurons on ITO glass ($n = 6$) and BHJs/$Ni_3(HITP)_2$ devices ($n = 6$). Boxes indicate 25th and 75th percentile, whiskers represent outliers (coefficient 1.5) and squares represent means. $P > 0.2$, Student's t-test. (c, e) Schematic representation of the hyperpolarization/rebound depolarization model showing membrane potential changes in cultured neurons on BHJs/$Ni_3(HITP)_2$ under low-intensity continuous (for inhibition) and high-intensity pulsed light (for excitation). Inhibition arises from the device polarity, which drives holes to the top surface of BHJs and accumulates anions at the cell interface. Excitation occurs via the rebound depolarization pathway involving Ca^{2+} influx potentially through T-type calcium channels. (d) Traces showing the inhibition of pre-excited rat DRG neurons by BHJs/$Ni_3(HITP)_2$ at relatively low light intensities. The neurons were initially excited by holding injected currents from pipette electrode, and were almost fully silenced during continuous illumination. The red shaded areas indicate the duration of continuous illumination at 25, 50, and 75 mW mm^{-2}. (f) Reproducible firing of cultured rat DRG neurons on BHJs/$Ni_3(HITP)_2$ devices with trains of light pulses (10 ms, 750 mW mm^{-2}) at (top) 1 and (bottom) 10 Hz. The red bars indicate the laser pulses.**

mimics the biofluids and surrounding environments for implantable devices (Figure 4b). This long-term stability against biofluids stems from the hydrophobicity of the selected BHJs materials, which has been considered a key factor for building stable organic photovoltaics.[49]

However, the hydrophobicity of BHJs-only devices hinders neuronal adhesion. Neurons fail to grow on the BHJs-only devices (PBDBT:ITIC, Figure S9), even with the assistance of a hydrophilic cell adhesion layer (such as poly D-lysine, or PDL). In contrast, $Ni_3(HITP)_2$ serves as an intermediate to bridge the hydrophobic BHJs and hydrophilic PDL layers. $Ni_3(HITP)_2$ can adhere well to BHJs. Based on previous reports on the $\pi-\pi$ interaction between conjugated BHJs and other functional materials containing conjugated moieties (carbon nanotubes[57,58] or MOFs),[59] the interaction between $Ni_3(HITP)_2$ and BHJs may involve $\pi-\pi$ interaction. It also integrates well with PDL through a combination of electrostatic interactions, improved surface wettability, and surface roughness. First, $Ni_3(HITP)_2$ is negatively charged at pH ≈ 7,[50] with a large ζ-potential (−40 mV), permitting electrostatic binding to the positively charged PDL (ζ-potential for PDL-coated $Ni_3(HITP)_2$ layer was more positive, −20 mV). Second, the $Ni_3(HITP)_2$ layer can substantially increase the surface wettability of the device (Figure 4c), transforming the hydrophobic BHJs (contact angle ≈103 °) to a more hydrophilic interface (contact angle ≈43°) suitable for PDL coating. Third, the $Ni_3(HITP)_2$ layer contains nanoscale porous structures with a relatively rough surface. The surface roughness estimated by atomic force microscopy (AFM) is about 26.1 nm (Figure 4d), compared to 3.8 nm in BHJs−only devices. The roughness is preferred for cell or tissue adhesion, because biological materials generally have rough surfaces.[17,30,51] These interactions

https://doi.org/10.1021/acsnano.5c01516
ACS Nano 2025, 19, 16813−16828

collectively result in a firmly bound PDL layer on the BHJs/$Ni_3(HITP)_2$ devices. Figure 4e shows the X-ray photoelectron spectroscopy (XPS) data in N 1s region measured from BHJs/$Ni_3(HITP)_2$ devices before and after PDL coating. To mimic the culturing conditions of neurons, the PDL-coated BHJs/$Ni_3(HITP)_2$ devices were immersed in PBS solution for 7 days before XPS measurement. Before PDL coating, the N 1s spectrum shows peaks corresponding to pyrrolic, pyridinic, and graphitic N in $Ni_3(HITP)_2$,[52] as indicated by the green, blue, and red shades in Figure 4e. After PDL coating and PBS immersion for 7 days, an additional component related to the amine groups in PDL (violet shaded area centered at ≈400.9 eV) is observed, confirming the strong binding of PDL on $Ni_3(HITP)_2$. Moreover, the PDL layer does not degrade the device performance. The photovoltage of BHJs/$Ni_3(HITP)_2$ devices retains about 96% of the initial value after PDL coating (Figure S8).

The PDL-coating renders BHJs/$Ni_3(HITP)_2$ suitable for forming tight and biocompatible junctions that promote neuronal adhesion and growth. To evaluate biocompatibility, we incubated mouse primary hippocampal neurons or rat dorsal root ganglion (DRG) neurons on ITO, BHJs-only, and BHJs/$Ni_3(HITP)_2$ devices. PDL coating was applied to all cases to enhance cell adhesion. PDL-coated ITO glass substrates, which are considered inert to neuronal growth, were used as control samples to assess the biocompatibility of organic bioelectronics.[18,38] Mouse primary hippocampal neurons cultured on BHJs/$Ni_3(HITP)_2$ devices for 10 days are virtually identical to those grown on PDL-coated ITO glass (Figures 4f and S9). Immunofluorescence imaging with a LIVE/DEAD Cell Imaging Kit (488/570) staining also shows no significant differences in cell viability for mouse hippocampal neurons (Figure 4f) or other cells (e.g., DRG neurons, Figures S11 and 12) cultured on ITO or BHJs/$Ni_3(HITP)_2$ devices. In contrast, only few neurons were observed on BHJs-only devices (Figure S9), probably due to mismatched surface hydrophilicity/hydrophobicity between the BHJs and PDL layers and the poor adhesion of neurons.

***In Vitro*, Bidirectional Photocapacitive Modulation of Neuronal Activity.** We then tested the ability of BHJs/$Ni_3(HITP)_2$ devices to promote or inhibit neuronal activity. We cultured rat DRG neurons on these devices (the BHJs layer contains PBDB-T and ITIC) and monitored the membrane potentials using whole-cell patch clamp recordings (Figure 5a). In the absence of illumination, cultured rat DRG neurons show an averaged resting membrane potential of about −50 mV, which is comparable with those grown on ITO substrates (Figure 5b). Under different illumination intensities, devices can either stimulate or suppress neuronal activity (Figure 5c,e). On the one hand, the activity of cultured DRG neurons (preactivated by injecting depolarizing current through the micropipette) can be fully suppressed when the devices are illuminated with low-intensity continuous light (25, 50, or 75 mW mm^{-2}, 5 s, Figure 5d). The hyperpolarization is exclusively attributed to the photocapacitive effect, as the action potentials recover immediately after illumination ceased. This inhibitory effect stems from the device polarity of PBDB-T:ITIC BHJs. Photogenerated holes accumulate at the biointerface, producing positive photovoltages and inducing anion accumulation near the cell membranes. This process reduces the membrane potential and causes hyperpolarization. On the other hand, a pulsed and intense excitation (≈10 ms, 750 mW mm^{-2}) applied to the same BHJs/$Ni_3(HITP)_2$ devices leads to elevated cell membrane potential (by over 40 mV, Figure S13a) and firing of spikes. The spikes can be elicited with trains of light pulses with great temporal precision and nearly 100% successful rate at frequencies of 1, 5, and 10 Hz (Figure 5f and S13b), which mimics the spike trains for neurons to process information.[53]

The observed bidirectional modulation of neuronal activity under illumination with low- and high-intensity light, as well as varying durations, can be explained by the hyperpolarization/rebound depolarization model.[55,56] This model predicts the hyperpolarization-to-depolarization transition by tuning the strength and duration of the applied potentials during electrical neuromodulation. In this model, relatively low positive electrode voltages can hyperpolarize the neurons, while higher positive voltages and pulsed stimulation can trigger a sequence of hyperpolarization, the return to resting potential, and the triggering of a large T-type Ca^{2+} influx to drive the rebound depolarization (Figure 5e). In our case, the low-intensity continuous illumination resembles the low-voltage electrical modulation. Under this condition, positive charges accumulate at the biointerface, inducing membrane hyperpolarization and inhibiting cellular activity (Figure 5c,d). Conversely, high-intensity pulsed light renders the membrane potential more positive, leading to a sequence of cellular hyperpolarization, cessation of the hyperpolarization, and rapid depolarization, potentially triggering an action potential (Figure 5e,f). Calcium imaging reveals enhanced fluorescence, confirming the occurrence of rebound depolarization (Figure S14).

It is important to note that both excitation and inhibition of neuronal activity are important for the normal functioning of the neuronal networks and the treatment of neurological disorders.[28] In our previous studies, we used inorganic, photoactive silicon p/n junctions to achieve bidirectional, nongenetic, and selective promotion and inhibition of neuronal activity. This was accomplished either by switching the configurations of p/n junctions[30] or by triggering photocapacitive inhibition or photothermal stimulation under different illumination modes.[31] In comparison, the bidirectional neuromodulation of our organic BHJs/$Ni_3(HITP)_2$ devices is achieved exclusively through photocapacitive hyperpolarization and rebound depolarization processes. To rule out any contribution from photothermal effects, we estimated the temperature increases near the BHJs/$Ni_3(HITP)_2$ device interface under both low- (for hyperpolarization, Figure S15a) and high-intensity illumination (for rebound depolarization, Figure S15b). For the high-intensity illumination case, we used a light intensity of 750 mW mm^{-2} (the same for the photostimulation experiments) to evaluate the photothermal effect. In both the low- and high-intensity illumination cases, the temperature increases under working conditions were negligible.

We also performed dynamic calcium imaging of cultured rat DRG and mouse primary hippocampal neurons on the BHJs/$Ni_3(HITP)_2$ devices to study photocapacitive modulation at a larger scale and with high spatial resolution (Figures S14, S16, and S17). In these cases, both types of neurons can be stimulated by pulsed irradiation from the laser source integrated in the confocal microscope, as evidenced by the several-fold increases in Ca^{2+} fluorescence intensity. Selective stimulation of a single neuron and monitoring the Ca^{2+} fluorescence intensity of its neighbors also reveal drastically different intercellular communication pathways (Ca^{2+} wave propagation or synaptic communication) in different types of neurons. Detailed results are provided in Figures S14, S16, and S17, and Movie S1 and related discussions in the Supporting Information. These results

https://doi.org/10.1021/acsnano.5c01516
ACS Nano 2025, 19, 16813−16828

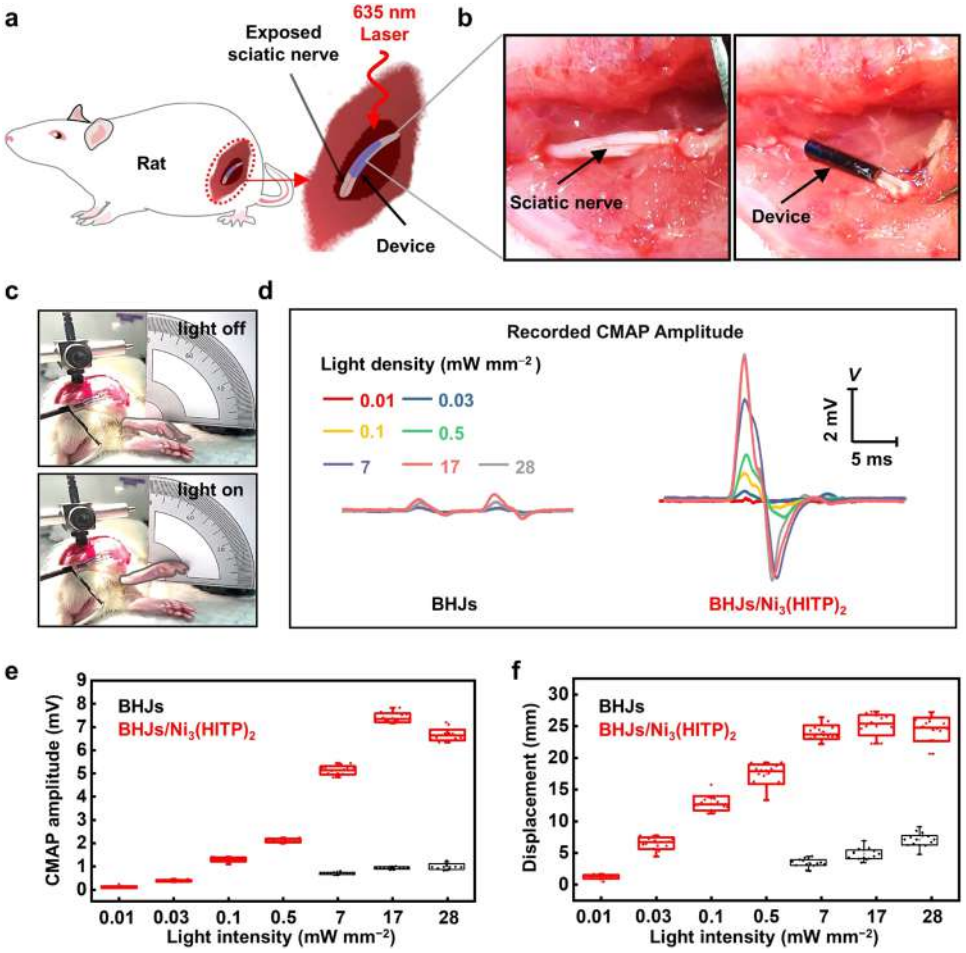

Figure 6. ***In vivo*** **peripheral neuromodulation using BHJs/$Ni_3(HITP)_2$ devices on rat models. (a) Schematic illustration of** ***in vivo*****, sciatic nerve stimulation in an anesthetized rat model using implantable BHJs/$Ni_3(HITP)_2$ photocapacitors under 635 nm illumination. (b) Photographs of the exposed sciatic nerve and the flexible BHJs/$Ni_3(HITP)_2$ devices conformally wrap around the exposed sciatic nerve and form intimate biointerface. (c) Photographs of rat hindlimb movement before and after photostimulation with implanted BHJs/$Ni_3(HITP)_2$ devices. (d) Typical CMAPs evoked by illuminating the BHJs-only or BHJs/$Ni_3(HITP)_2$ devices on one hindlimb of rat with various light intensities. Light pulse duration, 1 ms; frequency, 1 Hz. (e, f) Statistics of recorded (e) CMAP amplitudes near the sciatic nerve and (f) limb displacements of rats implanted with BHJs-only and BHJ/$Ni_3(HITP)_2$ devices, respectively, under various light intensities (pulse duration, 1 ms; frequency,1 Hz). The statistics were based on data collected during 12 pulses (n = 12). Box plots show the IQR centered around the median, with whiskers extending to 1.5 times the IQR above and below the box. Each illumination test was replicated more than twice on two separate rats.**

suggest that MOFs-modified BHJs devices can serve as a powerful platform to investigate and modulate the behavior of individual neurons and their networks with high spatiotemporal resolution.

In Vivo **Modulation of Peripheral Neuronal Activity.** Furthermore, BHJs/$Ni_3(HITP)_2$ devices enable wireless and nongenetic optoelectronic neuromodulation *in vivo*, with implications in neurodegenerative disease therapy and prosthetics. As a proof-of-concept, we employed a wild-type rat sciatic nerve model (Figure 6a) for peripheral nervous systems. In this case, devices were fabricated in the ultrathin (≈2 μm) and flexible form on polyimide substrates deposited with PEDOT:PSS@Ag nanowire electrodes. The flexible devices exhibit comparable performance to those made on ITO substrates, showing a photovoltage of about 70 mV, as measured via patch-clamp in PBS under a light intensity of 10 mW mm^{-2} (Figure S18a,b). To test the reliability of such flexible devices, we also made devices on poly(ethylene terephthalate) substrates, which can retain their photovoltage during bending, even at a bending angle of ≈160° (Figure S18c). After about 50 bending cycles (bending angle up to 160°), the devices preserve over 95% of their initial photovoltages (Figure S18d,e). When wrapped around the sciatic nerve (Figure 6b), the devices form conformal contact without using PDL layers, glues, or special fixation methods. The adhesion at the interface is likely due to the capillary interactions in the presence of water or van der Waals forces.[27] Interestingly, BHJs-only devices, when fabricated in flexible forms, can also be wrapped on the sciatic nerve, serving as a control to show the effects of $Ni_3(HITP)_2$ layer.

To quantify the effectiveness of *in vivo* neuromodulation, we placed electrodes to record evoked compound muscle action potentials (CMAPs) in the biceps femoris and used a camera to capture the displacements of hindlimb motion (Figures 6a and S19). Upon illumination of the biointerface, a significant displacement of the rat's hindlimb was observed, as illustrated in Figure 6c and Movie S2. Figure 6d compares the recorded CMAPs responses stimulated by BHJs-only and BHJs/$Ni_3(HITP)_2$ devices at various light intensities, while Figure 6e,f display the CMAPs and displacements of hindlimb motion from multiple measurements on different rats (n = 4). As

https://doi.org/10.1021/acsnano.5c01516
ACS Nano 2025, 19, 16813−16828

expected, both the CMAPs and motion amplitudes depended on the light intensities. When incident remotely with a pulsed laser beam (pulse width, 1 ms), BHJs-only devices generate small CMAPs (0.26 mV) and no observable hindlimb motion until light intensities reach a threshold of 7 mW mm^{-2}. The dual peaks with a decay <10 ms may be attributed to the simultaneous excitation of the faster- (e.g., Aα motor fibers) and slower-conducting (e.g., Aδ sensory or autonomic fibers) nerve fibers[60] due to the relatively large area of our devices. In comparison, BHJs/$Ni_3(HITP)_2$ devices can evoke hindlimb lifts with larger amplitude and higher CMAPs at significantly lower (by more than 2 orders of magnitude) light intensities. Even at an ultralow light intensity of about 0.01 mW mm^{-2}, a hindlimb lifting of 1.25 mm was observed, comparable to that triggered by BHJs-only devices illuminated at 7 mW mm^{-2}. At 0.1 mW mm^{-2}, the BHJs/$Ni_3(HITP)_2$ devices induced a motion over 1 cm and CMAP of ≈1.0 mV. We also measured the photovoltages of BHJs/$Ni_3(HITP)_2$ devices after the modulation experiment and recovered from the sciatic nerve. These devices show comparable photovoltages (Figure S20) and intact MOFs layer, primarily owing to their intimate contact with biotissues. Evaluating the long-term device stability and biocompatibility at the living animal level, which requires long-term implantation, is important for future studies. At 0.1 mW mm^{-2}, the BHJs/$Ni_3(HITP)_2$ devices induced a motion over 1 cm and CMAP of ≈1.0 mV. We further stimulated sciatic nerve and hindlimb motion of rats with PBDB-T:Y6/$Ni_3(HITP)_2$ devices under near-infrared light illumination. As shown in Figure S21, due to the great absorption of PBDB-T:Y6 in the near-infrared region, successful excitation was observed under relatively low laser intensity (808 nm, 0.3 mW mm^{-2}).

To place the discussion in the context of safe *in vivo* modulation, 635 nm light with intensities below the safety standards must be applied at the skin surface and transmit through tissue depths (≈6 mm in rats). We simulated light propagation and attenuation using a finite element analysis model (COMSOL Multiphysics v5.5) with the optical parameters of rat skins, fats, and muscles (Figure S22a). To achieve 1 mW mm^{-2} at a depth of 6 mm, which is sufficient to trigger CMAPs by BHJs/$Ni_3(HITP)_2$ devices according to Figure 6e,f, the required light intensity exposed to skin surface was calculated to be about 38 mW mm^{-2} (Figure S22b,c). These low-intensity pulses (pulse width, 1 ms) correspond to an energy density of 0.04 mJ cm^{-2}, which is 3−4 orders of magnitude lower than the accepted laser safety standards for skin exposure (e.g., the American National Safety Standard for the use of lasers, 195 mJ cm^{-2}). We note that the COMSOL simulation is based on simplified layered skin model and thus can only serve as a qualitative guidance. We also attempted to transdermally excite rat sciatic nerve. However, the intensity of our 635 nm laser (at its maximum power, ≈100 mW mm^{-2}) decayed significantly along the depth of 6 mm-thick tissue and became undetectable. These results confirm the limitation of COMSOL simulation due to the simplified model and suggest that we would need a more intense light source for transdermal stimulation. The COMSOL simulation on heat dissipation also provides estimated temperature increases induced by light exposure at the skin and deeper tissue layers (Figure S23). Short pulses (approximately 1 ms) with powers (e.g., 700 mW) applied to the skin surface for sciatic nerve stimulation cause minimal temperature rises (far below 1 °C).

CONCLUSIONS

In conclusion, we demonstrated the use of $Ni_3(HITP)_2$ MOFs as the interfacial layer between photocapacitive BHJs devices and cells or tissues to achieve effective nongenetic optical neuromodulation. The large capacitance, low impedance, and high porosity of the MOFs layer significantly increase the charge injection capacity and photovoltage, while enabling reliable binding at the biotic/abiotic interfaces. This strategy adapts well to the nonfullerene BHJs, such as PBDB-T:ITIC, as well as other high-performance photovoltaic BHJs, and thus facilitates their uses in effective photocapacitive modulation of cultured neurons and peripheral nerves in living animals under ultralow light intensity. These findings underscore the critical role of interfacial designs in optoelectronic devices for neuromodulation. Beside $Ni_3(HITP)_2$ reported here, other MOFs and other types of functional materials with suitable material properties, proper energy levels, and compatible processability with BHJs, can also be used. Rational designs of such interfacial materials can open up new opportunities to explore diverse BHJs compositions for the nongenetic modulation of neurons and other excitable biotissues, with applications in prosthetics and neurological disorder treatments.

EXPERIMENTAL SECTION

Chemicals and Materials. All reagents were purchased from commercial vendors and used without further purification. 2,3,6,7,10,11-hexaaminotriphenylene hexahydrochloride (HITP·6HCl, 98%) was purchased from Yanshen Technology Co., Ltd. $NiCl_2·6H_2O$ was purchased from Alfa Aesar. Ammonia−water ($NH_3·H_2O$, 28%) was purchased from Sinopharm Chemical Reagent Co., Ltd. Poly(3,4-ethylenedioxythiophene): poly(styrenesulfonate) (PEDOT:PSS, Clevios PH1000, 1.0−1.3 wt %) aqueous dispersion was purchased from Heraeus Ltd. Ethylene glycol (≥99%), 3-glycidoxypropyltrimethoxysilane (≥98%), chlorobenzene (≥98%) and chloroform (≥99%) were purchased from Sigma-Aldrich. PBDB-T (Poly-((2,6-(4,8-bis(5-(2-ethylhexyl)thiophen-2-yl)-benzo(1,2-b:4,5-b′)-dithiophene))-*alt*-(5,5-(1′,3′-di-2-thienyl-5′,7′-bis(2-ethylhexyl)-benzo(1′,2′-c:4′,5′-c′)dithiophene-4,8-dione))), ITIC (Indacenodithieno[3,2-*b*]thiophene-4,9-dione-2,6-bis(5-(2-ethylhexyl)thiophen-2-yl)benzo[1,2-b:4,5-b′]dithiophene), Y6 (2,2′-((2Z,2′Z)-((12,13-bis (2-ethylhexyl)-3,9-diundecyl-12,13-dihydro-(1,2,5) thiadiazolo (3,4-e) thieno (2′′,3′′′:4′′′,5′) thieno (2′,3′:4,5) pyrrolo (3,2-g) thieno (2′,3′:4,5) thieno (3,2-b) indole-2,10-diyl) bis (methanylylidene))) bis (5,6-difluoro-3-oxo-2,3-dihydro-1*H*-inden-2,1-diylidene)) dimalononitrile), PTB7-Th (Poly(4,8-bis(5-(2-ethylhexyl)thiophen-2-yl)benzo(1,2-b;4,5-b′)dithiophene-2,6-diyl-*alt*-(4-(2-ethylhexyl)-3-fluorothieno(3,4-b)thiophene-)-2-carboxylate-2,6-diyl)), P3HT (Poly(3-hexylthiophene-2,5-diyl)), PCBM ((6,6)-Phenyl-C61-butyric acid methyl ester) and all other donors and acceptors for BHJs were purchased from Solarmer Ltd. Ag nanowires (10 mg mL^{-1} concentration in aqueous solvent) and polyimide (ZKPI-3020, 16% solids) were purchased from Zhejiang Kechuang Advanced Materials Technology Co., Ltd. and Beijing POME Technology Co., Ltd., respectively.

Synthesis of $Ni_3(HITP)_2$ MOFs. The $Ni_3(HITP)_2$ MOFs film was prepared at the air−liquid interface following a previous report,[53,54] with some modifications. 2.5 mL of aqueous HITP·6HCl solution (1 mg mL^{-1}) and 2.5 mL of $NiCl_2·6H_2O$ (0.64 mg mL^{-1}) were sequentially added to 5 mL of H_2O in a 20 mL beaker (diameter, 30 mm). The beaker was placed on a hot plate and heated to 60 °C. Subsequently, 50 μL of $NH_3·H_2O$ (28%) was added dropwise to the surface of the mixed solution. A $Ni_3(HITP)_2$ film with a thickness of 30 nm formed at the air−liquid interface after 15 min.

Fabrication of BHJs/$Ni_3(HITP)_2$ and BHJs-only Devices. BHJs/$Ni_3(HITP)_2$ and BHJs-only devices were fabricated on ITO glass or polyimide substrate. The ITO glass substrates were sonicated sequentially in detergent solution, deionized water, and ethanol (15

https://doi.org/10.1021/acsnano.5c01516
ACS Nano 2025, 19, 16813−16828

min for each step). Before device fabrication, the cleaned substrates were heated at 150 °C for 30 min to remove the moisture. For BHJs-only device, the BHJs solution (18 mg mL^{-1}, comprising PBDB-T and ITIC in chlorobenzene with a mass ratio of 1:1) was spin-coated (2000 rpm, 40 s) onto the ITO substrates and annealed at 100 °C for 10 min. Devices of BHJs with other compositions (e.g., PTB7-Th: ITIC, PBDB-T: N2200, PBDB-T: IDIC) were made under the same conditions. For PBDB-T: Y6 devices, the solution (7 mg mL^{-1}, comprising PBDB-T and Y6 in chloroform with a mass ratio of 1:1) was spin-coated (2500 rpm, 40 s) on the ITO substrates and annealed at 100 °C for 10 min. The thickness of PBDB-T: ITIC, PTB7-Th: ITIC, PBDB-T: N2200, and PBDB-T: IDIC was approximately 100 nm, while that of PBDB-T: Y6 was around 50 nm. The area of the spin-coated BHJs layer was about 9 mm^2. To fabricate BHJs/$Ni_3(HITP)_2$ devices, the coated BHJs layer (facing down) was slowly stamped onto the $Ni_3(HITP)_2$ film formed at the air−liquid interface using the Langmuir-Schäfer transfer method,[45,54] as shown in Figure S1. This process transferred the $Ni_3(HITP)_2$ film onto the BHJs layer. The resulting BHJs/$Ni_3(HITP)_2$ devices were then rinsed with deionized water and ethanol to remove residual impurities. Before use, both BHJs/$Ni_3(HITP)_2$ and BHJs-only devices were vacuum-dried for at least 12 h to remove residual solvent.

Flexible BHJs/$Ni_3(HITP)_2$ and BHJs-only devices were fabricated on polyimide substrates. A fluorinated polymer layer (Novec 1700, 3M) was spin-coated on the cleaned glass substrate (4000 rpm, 60 s) and rinsed with acetone to remove excessive fluorinated polymers. A 2-μm-thick polyimide film was then spin-coated (4000 rpm, 60 s) onto the fluorinated glass substrate, annealed at 200 °C for 1 h in nitrogen, and soaked in water overnight to facilitate delamination from the glass substrates. An aqueous solution of PEDOT:PSS (1.0−1.3 wt %, with 5 wt % ethylene glycol and 1 wt % 3-glycidoxypropyltrimethoxysilane as cross-linker) was mixed with an aqueous solution of Ag nanowires (10 mg mL^{-1}) with the volume ratio of 1:1 by vertexing. The mixed solution was spin-coated (1500 rpm, 60 s) on the polyimide-coated glass substrate, annealed at 180 °C for 30 min, and rinsed with water. Subsequently, the BHJs and $Ni_3(HITP)_2$ layers were deposited and stamp-transferred following the same procedures described for making the rigid devices. Finally, the flexible BHJs/$Ni_3(HITP)_2$ or BHJs-only devices on polyimide substrates were obtained by carefully delaminating them from the glass substrates.

Characterization Techniques for Materials. UV−visible absorption spectra of BHJs and $Ni_3(HITP)_2$ films were measured in transmission mode with an Agilent Cary 5000 UV−vis-NIR spectrophotometer. Cyclic voltammetry and electrochemical impedance spectroscopy data were obtained using a CHI 660b instrument and PARSTAT 2273 potentiostat/galvanostat instrument, respectively. Atomic force microscopy (AFM) images were taken in the ScanAsyst mode on Oxford Cypher 5. Scanning Kelvin Probe Force Microscopy (SKPFM) measurements were carried out under ambient conditions using a Dimension Icon Scanning Probe Microscope (Bruker Nano, Inc.). The system was operated in single-pass frequency-modulated mode to achieve high-resolution mapping of both topography and surface potential. X-ray photoelectron spectroscopy (XPS) and ultraviolet photoemission spectroscopy (UPS) measurements of ITO and $Ni_3(HITP)_2$ films used a ThermoFisher Scientific ESCALAB Xi+ spectrometer with a monochromatic He I (21.2 eV) source. The samples were deposited on the ITO glass by spin-coating or stamp transfer-printing. Surface ζ-potential measurements were performed on films in PBS buffer solution using an Anton Paar SurPASS 3 instrument. Water contact angles were measured on a Dataphysics OCA25 instrument.

Optoelectronic Characterizations of Devices. The photo-induced voltages of BHJs-only and BHJs/$Ni_3(HITP)_2$ devices were recorded using a patch-clamp setup. The devices were fully immersed in PBS solution, and glass pipettes (≈1−5 MΩ) filled with 1× PBS solution were positioned at a distance of ≈10 μm from the device surface. A red laser beam (peak wavelength 635 nm, spot size ≈4 mm, in pulse mode, light intensity 20 mW mm^{-2}) was incident on the device surface through a collimating lens. Data recording was performed in voltage-clamp mode using an Axopatch 200B amplifier controlled by pClamp software (Molecular Devices). Signals were filtered at 10 kHz and sampled at 200 kHz.

Evaluation of the Photothermal Effect of Devices under Continuous and Pulsed Illumination. The photothermal effect of BHJs/$Ni_3(HITP)_2$ devices immersed in PBS solution under continuous illumination was measured using a thermocouple (USB-TC01, National Instruments Co.). The thermocouple was positioned on the surface of the devices. A 635 nm laser with a spot radius of 2 mm was used as the light source, and the temperature at various laser power densities was recorded.

The photothermal effect of devices immersed in PBS solution under pulsed illumination was evaluated using a micropipette method in voltage-clamp mode.[10] Temperature increases in the electrolytes enhance ion mobility and reduce pipette tip resistance. Consequently, under a constant holding potential V_p, the current would rise if a photothermal effect is present. The thermal current $\Delta I_{thermal}(t)$ is significantly influenced by the holding potential V_p and the baseline current I_0. Since the electrical current $\Delta I_{electric}(t)$ and the thermally induced current $\Delta I_{thermal}(t)$ exhibit markedly different dependencies on the holding potential V_0, the total photogenerated current $\Delta I_{light}(t) = \Delta I_{electric}(t) + \Delta I_{thermal}(t)$ can be decoupled by analyzing current traces recorded at various holding potentials. At any given time point t during the light illumination period, the recorded current $I_0 + \Delta I_{light}(t)$, excluding the photoelectrically induced current component $\Delta I_{electric}(t)$, follows Ohm's law in conjunction with the pipette tip resistance $R(t)$, provided the holding potential V_p remains fixed.

$$V_p = I_0 \times R_0 = (I_0 + \Delta I_{light}(t) - \Delta I_{electric}(t)) \times R \quad (2)$$

Rearranging eq 1 yields the relationship between the light-induced current $\Delta I_{light}(t)$ and the holding current I_0 as follows

$$\Delta I_{light}(t) = \left(\frac{R_0}{R(t)} - 1\right) \times I_0 + \Delta I_{electric}(t) \quad (3)$$

As demonstrated by eq 3, the photoelectric effect is explicitly represented by the intercept of the curve.

In this work, a 10 ms illumination period was applied to stimulate neuronal activity, and $\Delta I_{light,10\ ms}-I_0$ plots were used to evaluate the photothermal responses of the BHJs/$Ni_3(HITP)_2$ devices. If device has only the photoelectric effect without any photothermal effect, that is, $R_0 = R_{10\ ms}$, eq 3 can be written as

$$\Delta I_{light} = \Delta I_{electric} \quad (4)$$

The $\Delta I_{light,10\ ms} - I_0$ plot will be a horizontal line with a zero or minimal intercept.

Culture of Rats DRG Neurons. DRG neurons from male rats (4 weeks) were extracted and transferred into a tube containing 1 mL of ice-cold of Dulbecoo's modified Eagle medium/nutrient mixture F-12 (DMEM/F12, Gibco) with 1% penicillin−streptomycin solution (Gibco). The tissues were cut into small pieces and treated with an enzyme solution containing 5 mg mL^{-1} Dispase (ST2339, Beyotime Biotechnology) and 1 mg mL^{-1} collagenase (ST2294, Beyotime) at 37 °C for 1 h. After trituration (with 1 mL pipette for ≈30 times, until the liquid became turbid) and centrifugation (250g, 5 min), cells were washed in 15% (w/v) bovine serum albumin (Sigma-Aldrich) and resuspended in 2 mL of DMEM/F12 containing 10% fetal bovine serum and 1% penicillin−streptomycin. Prior to cell seeding, the BHJs/$Ni_3(HITP)_2$ devices were sterilized with 70% ethanol and exposed to UV light for 30 min. The devices were then coated by immersion in a poly-D-lysine solution (0.25 mg mL^{-1}, Sigma-Aldrich) for 8 h. One-tenth of the total DRG cells was seeded on the devices in each well of the 24-well plate. The DRG cells were cultured in an incubator at 37 °C for 1 day.

Culture of Mouse Primary Hippocampal Neurons. To culture primary hippocampal neurons, hippocampal tissue was dissected from postnatal day 0 (P0) mice using Hank's balanced salt solution (Life Technologies) supplemented with 5 mM HEPES (Life Technologies) and 20 mM D-glucose (Life Technologies) under a dissecting microscope. The tissue was digested with 0.25% trypsin (Life Technologies) for 10 min at 37 °C and subsequently washed with

https://doi.org/10.1021/acsnano.5c01516
ACS Nano 2025, 19, 16813−16828

Dulbecco's Modified Eagle's Medium (DMEM, Life Technologies) containing 2% fetal bovine serum (FBS, Life Technologies). The isolated cells were cultured in Neurobasal A medium supplemented with 2% B27 (Life Technologies), 2 mM GlutaMax (Life Technologies), and 1% penicillin-streptomycin (P/S, Life Technologies). Prior to cell seeding, the BHJs/$Ni_3(HITP)_2$ devices were sterilized with 70% ethanol and exposed to UV light for 30 min. The devices were then coated by immersion in a poly-D-lysine solution (0.25 mg mL^{-1}, Sigma-Aldrich) for 8 h. The hippocampal neurons were seeded onto the prepared device films at a density of 50,000 to 100,000 cells per cm^2 and incubated for 7 days.

Cell Viability Tests. To evaluate the viability of neurons cultured on BHJs/$Ni_3(HITP)_2$ devices and ITO glass, fluorescence imaging was performed using a LIVE/DEAD Cell Imaging Kit (488/570, Life Technologies). After three washes with Hank's balanced salt solution containing 20 mM HEPES (HHBS, Life Technologies), live cells were stained with Calcein AM (green), dead cells with EthD-1 (red), and nuclei with Hoechst 33342 (blue). The cells were incubated in the staining solution for 15 min at room temperature, and images were captured using a Nikon AXR NSPARC confocal microscope.

***In Vitro* Optical Neuromodulation and Electrophysiological Recording.** DRG neurons were perfused with artificial cerebrospinal fluid (ACSF, Life Technologies) containing 126 mM NaCl, 3 mM KCl, 1 mM $MgCl_2$, 2.5 mM $CaCl_2$, 10 mM glucose, 26 mM $NaHCO_3$ and 1.2 mM NaH_2PO_4 at room temperature. Recording pipettes (6−7 MΩ) were pulled using a micropipette puller (P1000, Sutter Instrument). For whole-cell recordings, pipettes were filled with internal solution containing 120 mM K-gluconate, 10 mM HEPES, 0.2 mM EGTA, 2 mM KCl, 4 mM Na_2ATP, 0.4 mM Na_2GTP, 2 mM $MgCl_2$ and 10 mM Na_2phosphocreatine (pH 7.2−7.4). Light stimulations were generated using a 635 nm laser (MDL-D-635 nm, Changchun New Industries Optoelectronics Tech. Co., Ltd.) with power, frequency, and duration controlled. The laser beam, adjustable from 2 to 500 μm in spot size, was delivered to the devices via an optical fiber with a 200 μm diameter. The light pulses were synchronized with patch clamp logic signals, and the intensity at the fiber terminus was quantified using a power meter (LP10, Sanwa). Voltage- and current-clamp recordings were performed with a computer-controlled amplifier (MultiClamp 700B, Molecular Devices). Recorded data were low-pass filtered at 3 kHz and sampled at 10 kHz (DigiData 1440, Molecular Devices), and data analysis was performed using Clampfit 10 software (Molecular Devices).

Calcium Imaging during the Optical Neuromodulation. For staining both mouse primary hippocampal neurons and rat dorsal root ganglion neurons cultured on devices, Calbryte-520 (Screen Quest Calbryte-520 Probenecid-Free and Wash-Free Calcium Assay Kit, AAT-A36317) was utilized as a fluorescent calcium indicator. Specifically, 50 μg of Calbryte-520 AM was dissolved in 45.8 μL of dimethyl sulfoxide (DMSO) and stored at −20 °C. The cells were washed three times with HHBS solution, then incubated with a solution containing 4 μL of the Calbryte-520 AM stock diluted in 1 mL of HHBS buffer for 30 min. Following this incubation, the cells were washed three times and further incubated in HHBS solution for an additional 30 min.

Ca^{2+} fluorescent signals were imaged using a 20× objective on an inverted confocal microscope (Nikon AXR NSPARC). The stimulation laser was tuned to 640 nm, while a 488 nm laser was used to image the region of interest. Prior to stimulation, fluorescent images were captured for ≈50 s to collect the baseline. The 640 nm laser was then activated, and the fluorescent images were acquired for the stimulated neurons over a 10 s period. The 640 nm laser had a power of 2 mW. Fluorescence images were analyzed using ImageJ. Normalized fluorescence changes were calculated as $\Delta F/F_0 = (F - F_0)/F_0$, where F_0 is the baseline intensity.

***In Vivo* Optical Neuromodulation of the Sciatic Nerve in Rats.** Wild-type rats (C57BL/6, 6 weeks old, purchased from VitalRiver) were used for the experiments. Rats were anesthetized with 2% isoflurane in balanced oxygen before the operation. The fur on hindquarters was removed using surgical clippers. The sciatic nerve was then exposed by carefully releasing the surrounding connective tissue. BHJs-only and BHJs/$Ni_3(HITP)_2$ devices fabricated on flexible polyimide substrates were wrapped around the nerve surface to establish firm contact without the need for glues or additional fixation. A red laser beam (635 nm, spot size ≈4 mm) was illuminated on the device/nerve interface using a collimating lens. Electromyographic (EMG) signals and hindlimb movements were recorded during the illumination. For evoked compound muscle action potentials (CMAPs) recordings, an electrophysiology multichannel recording and processing system (Chengdu Instrument Factory, RM6240E/EC) was used. The recording electrode was inserted into the tibial muscle region, and CMAPs were recorded using a low-pass filter of 300 Hz. The limb movements were captured with a camera at a speed of 30 frames per second.

Simulation of Light Penetration Depths and Photothermal Effect in Animals. The simulation was conducted using the "Absorption-Scattering" and "Bioheat-Transfer" coupling multiphysics in COMSOL.[27] Parameters of rat skin and tissue used in the model were as follows: skin density, 1.1 g cm^{-3}; thermal conductivity, 0.37 W m^{-1} K^{-1}; heat capacity, 3.4 J g^{-1} K^{-1}; and optical absorption and scattering coefficients at 635 nm, 50 and 2500 m^{-1}, respectively. A 635 nm laser beam (power density, 700 mW cm^{-2}; spot size, 4 mm; pulse frequency, 1 Hz; duration, 1 ms) was set as the light and heat source. The heat transfer boundary condition for skin (37 °C) to air (25 °C) was defined as convective heat flux.

Animal Care. All animal protocols adhered to the guidelines provided by the National Institute of Biological Sciences in Beijing and Tsinghua University, and were approved by Institutional Animal Care and Use Committee.

ASSOCIATED CONTENT

Supporting Information

The Supporting Information is available free of charge at https://pubs.acs.org/doi/10.1021/acsnano.5c01516.

Preparation process of BHJs/$Ni_3(HITP)_2$ devices; optical transmittance and UPS spectrum of $Ni_3(HITP)_2$; cyclic voltammetry of BHJ-only and BHJs/$Ni_3(HITP)_2$ devices; additional photovoltage tests of BHJs/$Ni_3(HITP)_2$ devices; photovoltage traces recorded from PBDB-T:ITIC and PBDB-T:ITIC/$Ni_3(HITP)_2$ devices under the irradiation of lasers with wavelengths of 470, 635, and 808 nm; molecular formulas of other BHJs donors and acceptors; optical microscopic images of mouse primary hippocampal neurons cultured on different substrates; cell biocompatibility of MCF7 cells and rat DRG cells cultured on BHJs/$Ni_3(HITP)_2$ devices; additional electrophysiological data of rat DRG cells stimulated by pulsed light on BHJs/$Ni_3(HITP)_2$ devices; calcium imaging of cultured neurons optically modulated by BHJs/$Ni_3(HITP)_2$ devices; calcium dynamics of mouse primary hippocampal neurons cultured on ITO glass and glass under illumination (as a control group); evaluation of the photothermal effect of BHJs/$Ni_3(HITP)_2$ devices; photoresponse of BHJs/$Ni_3(HITP)_2$ devices fabricated on the flexible polyimide substrate; photovoltage of BHJ/$Ni_3(HITP)_2$ devices before and after the *in vivo* rat sciatic nerve modulation experiment; *in vivo* peripheral neuromodulation using PBDB-T:Y6/$Ni_3(HITP)_2$ devices on rat models under 808 nm near-infrared light; simulation of light intensity decay along the depths of rat skin and tissue (PDF)

Ca^{2+} imaging during photostimulation of cultured mouse hippocampal neurons and rat DRG neurons by BHJs/$Ni_3(HITP)_2$ devices (Movie S1) (MP4)

Recorded rat hindlimb movement during the photostimulation of sciatic nerve by BHJs/$Ni_3(HITP)_2$ devices (Movie S2) (MP4)

https://doi.org/10.1021/acsnano.5c01516
ACS Nano 2025, 19, 16813−16828

AUTHOR INFORMATION

Corresponding Authors

Jun Yao − *State Key Laboratory of Membrane Biology, IDG/McGovern Institute for Brain Research, School of Life Sciences, Tsinghua University, Beijing 100084, China*; Email: jyao@mail.tsinghua.edu.cn

Xing Sheng − *Department of Electronic Engineering, Beijing National Research Center for Information Science and Technology, Institute for Precision Medicine, Laboratory of Flexible Electronics Technology, IDG/McGovern Institute for Brain Research, Tsinghua University, Beijing 100084, China*; orcid.org/0000-0002-8744-1700; Email: xingsheng@mail.tsinghua.edu.cn

Jinghong Li − *Department of Chemistry, Center for Bioanalytical Chemistry, Key Laboratory of Bioorganic Phosphorus Chemistry & Chemical Biology (Ministry of Education), Tsinghua University, Beijing 100084, China*; orcid.org/0000-0002-0750-7352; Email: jhli@mail.tsinghua.edu.cn

Hao Zhang − *Department of Chemistry, Center for Bioanalytical Chemistry, Key Laboratory of Bioorganic Phosphorus Chemistry & Chemical Biology (Ministry of Education), Tsinghua University, Beijing 100084, China*; orcid.org/0000-0003-4513-0813; Email: hzhangchem@mail.tsinghua.edu.cn

Authors

Kangkang Weng − *Department of Chemistry, Center for Bioanalytical Chemistry, Key Laboratory of Bioorganic Phosphorus Chemistry & Chemical Biology (Ministry of Education), Tsinghua University, Beijing 100084, China; School of Optics and Photonics, Beijing Key Laboratory for Precision Optoelectronic Measurement Instrument and Technology, Beijing Institute of Technology, Beijing 100081, China*

Wenjun Li − *Department of Chemistry, Center for Bioanalytical Chemistry, Key Laboratory of Bioorganic Phosphorus Chemistry & Chemical Biology (Ministry of Education), Tsinghua University, Beijing 100084, China*

Xinyu Cheng − *Department of Chemistry, Center for Bioanalytical Chemistry, Key Laboratory of Bioorganic Phosphorus Chemistry & Chemical Biology (Ministry of Education), Tsinghua University, Beijing 100084, China*; orcid.org/0009-0008-1711-3366

Yunyun Xing − *State Key Laboratory of Membrane Biology, IDG/McGovern Institute for Brain Research, School of Life Sciences, Tsinghua University, Beijing 100084, China*

Xin Fu − *Department of Electronic Engineering, Beijing National Research Center for Information Science and Technology, Institute for Precision Medicine, Laboratory of Flexible Electronics Technology, IDG/McGovern Institute for Brain Research, Tsinghua University, Beijing 100084, China*

Yinghan Wang − *State Key Laboratory of Membrane Biology, IDG/McGovern Institute for Brain Research, School of Life Sciences, Tsinghua University, Beijing 100084, China*

Huachun Wang − *Department of Electronic Engineering, Beijing National Research Center for Information Science and Technology, Institute for Precision Medicine, Laboratory of Flexible Electronics Technology, IDG/McGovern Institute for Brain Research, Tsinghua University, Beijing 100084, China*

Xiaoli Tian − *Department of Chemistry, Center for Bioanalytical Chemistry, Key Laboratory of Bioorganic Phosphorus Chemistry & Chemical Biology (Ministry of Education), Tsinghua University, Beijing 100084, China*

Yuqi Wang − *Department of Electronic Engineering, Beijing National Research Center for Information Science and Technology, Institute for Precision Medicine, Laboratory of Flexible Electronics Technology, IDG/McGovern Institute for Brain Research, Tsinghua University, Beijing 100084, China*

Lizhu Li − *Department of Electronic Engineering, Beijing National Research Center for Information Science and Technology, Institute for Precision Medicine, Laboratory of Flexible Electronics Technology, IDG/McGovern Institute for Brain Research, Tsinghua University, Beijing 100084, China; Sichuan Provincial Key Laboratory for Human Disease Gene Study and the Center for Medical Genetics, School of Life Science and Technology, University of Electronic Science and Technology of China, Chengdu 611731, China*

Complete contact information is available at: https://pubs.acs.org/10.1021/acsnano.5c01516

Author Contributions

[#]K.W., W.L., X.C., and Y.X. contributed equally to this work. All authors have given approval to the final version of the manuscript.

Notes

The authors declare no competing financial interest.

ACKNOWLEDGMENTS

This work was financially supported by the Beijing Natural Science Foundation (No. JQ24003, H.Z.), National Key Research and Development Program of China (No. 2022YEA1206101, H.Z.), National Natural Science Foundation of China (No. 22274087, H.Z.; Nos. T2425003 and 52272277, X.S.; Nos. 32371008 and 31830038, J.Y.), Tsinghua University Dushi Program (H.Z.), Beijing Natural Science Foundation (No. Z210011, J.Y.), China Postdoctoral Science Foundation (Nos. 2021TQ0168 and 2021M691758, K.W.), and 2022 Doctoral/Postdoctoral Project Application Report For Brain+X Seed Grant Program (Y.W. and K.W.)

REFERENCES

(1) Won, S. M.; Song, E.; Reeder, J. T.; Rogers, J. A. Emerging Modalities and Implantable Technologies for Neuromodulation. *Cell* **2020**, *181* (1), 115−135.

(2) Tian, B.; Xu, S.; Rogers, J. A.; Cestellos-Blanco, S.; Yang, P.; Carvalho-de-Souza, J. L.; Bezanilla, F.; Liu, J.; Bao, Z.; Hjort, M.; Cao, Y.; Melosh, N.; Lanzani, G.; Benfenati, F.; et al. Roadmap on semiconductor-cell biointerfaces. *Phys. Biol.* **2017**, *15* (3), No. 031002, DOI: 10.1088/1478-3975/aa9f34.

(3) Chen, R.; Canales, A.; Anikeeva, P. Neural recording and modulation technologies. *Nat. Rev. Mater.* **2017**, *2* (2), No. 16093.

(4) Tian, B. Nongenetic neural control with light. *Science* **2019**, *365* (6452), 457.

(5) Benfenati, F.; Lanzani, G. Clinical translation of nanoparticles for neural stimulation. *Nat. Rev. Mater.* **2021**, *6* (1), 1−4.

(6) Tian, B.; Lieber, C. M. Nanowired Bioelectric Interfaces. *Chem. Rev.* **2019**, *119* (15), 9136−9152.

(7) Cui, H.; Zhao, S.; Hong, G. Wireless deep-brain neuromodulation using photovoltaics in the second near-infrared spectrum. *Device* **2023**, *1* (4), No. 100113.

(8) Parameswaran, R.; Carvalho-de-Souza, J. L.; Jiang, Y.; Burke, M. J.; Zimmerman, J. F.; Koehler, K.; Phillips, A. W.; Yi, J.; Adams, E. J.; Bezanilla, F.; Tian, B. Photoelectrochemical modulation of neuronal activity with free-standing coaxial silicon nanowires. *Nat. Nanotechnol.* **2018**, *13* (3), 260−266.

(9) Tye, K. M.; Deisseroth, K. Optogenetic investigation of neural circuits underlying brain disease in animal models. *Nat. Rev. Neurosci.* **2012**, *13* (4), 251−266.
(10) Jiang, Y.; Li, X.; Liu, B.; Yi, J.; Fang, Y.; Shi, F.; Gao, X.; Sudzilovsky, E.; Parameswaran, R.; Koehler, K.; et al. Rational design of silicon structures for optically controlled multiscale biointerfaces. *Nat. Biomed. Eng.* **2018**, *2* (7), 508−521.
(11) Jiang, Y.; Tian, B. Inorganic semiconductor biointerfaces. *Nat. Rev. Mater.* **2018**, *3* (12), 473−490.
(12) Schaumann, E. N.; Tian, B. Biological Interfaces, Modulation, and Sensing with Inorganic Nano-Bioelectronic Materials. *Small Methods* **2020**, *4* (5), No. 1900868.
(13) Focus on neuroscience methods *Nat. Neurosci.* 2020; Vol. *23* 12, pp 1455−1455.
(14) Simon, D. T.; Gabrielsson, E. O.; Tybrandt, K.; Berggren, M. Organic Bioelectronics: Bridging the Signaling Gap between Biology and Technology. *Chem. Rev.* **2016**, *116* (21), 13009−13041.
(15) Rivnay, J.; Owens, R. M.; Malliaras, G. G. The Rise of Organic Bioelectronics. *Chem. Mater.* **2014**, *26* (1), 679−685.
(16) Ledesma, H. A.; Li, X.; Carvalho-de-Souza, J. L.; Wei, W.; Bezanilla, F.; Tian, B. An atlas of nano-enabled neural interfaces. *Nat. Nanotechnol.* **2019**, *14* (7), 645−657.
(17) Fang, Y.; Meng, L.; Prominski, A.; Schaumann, E. N.; Seebald, M.; Tian, B. Recent advances in bioelectronics chemistry. *Chem. Soc. Rev.* **2020**, *49* (22), 7978−8035.
(18) Ghezzi, D.; Antognazza, M. R.; Dal Maschio, M.; Lanzarini, E.; Benfenati, F.; Lanzani, G. A hybrid bioorganic interface for neuronal photoactivation. *Nat. Commun.* **2011**, *2* (1), No. 166.
(19) Ghezzi, D.; Antognazza, M. R.; Maccarone, R.; Bellani, S.; Lanzarini, E.; Martino, N.; Mete, M.; Pertile, G.; Bisti, S.; Lanzani, G.; Benfenati, F. A polymer optoelectronic interface restores light sensitivity in blind rat retinas. *Nat. Photonics* **2013**, *7* (5), 400−406.
(20) Benfenati, V.; Martino, N.; Antognazza, M. R.; Pistone, A.; Toffanin, S.; Ferroni, S.; Lanzani, G.; Muccini, M. Organic Polymers: Photostimulation of Whole-Cell Conductance in Primary Rat Neocortical Astrocytes Mediated by Organic Semiconducting Thin Films (Adv. Healthcare Mater. 3/2014). *Adv. Healthcare Mater.* **2014**, *3* (3), 306.
(21) Gautam, V.; Rand, D.; Hanein, Y.; Narayan, K. S. A Polymer Optoelectronic Interface Provides Visual Cues to a Blind Retina. *Adv. Mater.* **2014**, *26* (11), 1751−1756.
(22) Martino, N.; Feyen, P.; Porro, M.; Bossio, C.; Zucchetti, E.; Ghezzi, D.; Benfenati, F.; Lanzani, G.; Antognazza, M. R. Photothermal cellular stimulation in functional bio-polymer interfaces. *Sci. Rep.* **2015**, *5* (1), No. 8911.
(23) Rand, D.; Jakešová, M.; Lubin, G.; Vėbraitė, I.; David-Pur, M.; Đerek, V.; Cramer, T.; Sariciftci, N. S.; Hanein, Y.; Głowacki, E. D. Direct Electrical Neurostimulation with Organic Pigment Photocapacitors. *Adv. Mater.* **2018**, *30* (25), No. 1707292.
(24) Jakešová, M.; Ejneby, M. S.; Đerek, V.; Schmidt, T.; Gryszel, M.; Brask, J.; Schindl, R.; Simon, D. T.; Berggren, M.; Elinder, F.; et al. Optoelectronic control of single cells using organic photocapacitors. *Sci. Adv.* **2019**, *5* (4), No. eaav5265.
(25) Maya-Vetencourt, J. F.; Ghezzi, D.; Antognazza, M. R.; Colombo, E.; Mete, M.; Feyen, P.; Desii, A.; Buschiazzo, A.; Di Paolo, M.; Di Marco, S.; et al. A fully organic retinal prosthesis restores vision in a rat model of degenerative blindness. *Nat. Mater.* **2017**, *16* (6), 681−689.
(26) Ferlauto, L.; Leccardi, M. J. I. A.; Chenais, N. A. L.; Gilliéron, S. C. A.; Vagni, P.; Bevilacqua, M.; Wolfensberger, T. J.; Sivula, K.; Ghezzi, D. Design and validation of a foldable and photovoltaic wide-field epiretinal prosthesis. *Nat. Commun.* **2018**, *9* (1), No. 992.
(27) Ejneby, M. S.; Jakešová, M.; Ferrero, J. J.; Migliaccio, L.; Sahalianov, I.; Zhao, Z.; Berggren, M.; Khodagholy, D.; Đerek, V.; Gelinas, J. N.; Głowacki, E. D. Chronic electrical stimulation of peripheral nerves via deep-red light transduced by an implanted organic photocapacitor. *Nat. Biomed. Eng.* **2022**, *6* (6), 741−753.
(28) Huang, Y.; Cui, Y.; Deng, H.; Wang, J.; Hong, R.; Hu, S.; Hou, H.; Dong, Y.; Wang, H.; Chen, J.; et al. Bioresorbable thin-film silicon diodes for the optoelectronic excitation and inhibition of neural activities. *Nat. Biomed. Eng.* **2023**, *7* (4), 486−498.
(29) Fu, X.; Hu, Z.; Li, W.; Ma, L.; Chen, J.; Liu, M.; Liu, J.; Hu, S.; Wang, H.; Huang, Y.; et al. A silicon diode−based optoelectronic interface for bidirectional neural modulation. *Proc. Natl. Acad. Sci. U.S.A.* **2024**, *121* (30), No. e2404164121.
(30) Abdullaeva, O. S.; Schulz, M.; Balzer, F.; Parisi, J.; Lützen, A.; Dedek, K.; Schiek, M. Photoelectrical Stimulation of Neuronal Cells by an Organic Semiconductor−Electrolyte Interface. *Langmuir* **2016**, *32* (33), 8533−8542.
(31) Medagoda, D. I.; Ghezzi, D. Organic semiconductors for light-mediated neuromodulation. *Commun. Mater.* **2021**, *2* (1), No. 111.
(32) Savva, A.; Hama, A.; Herrera-López, G.; Schmidt, T.; Migliaccio, L.; Steiner, N.; Kawan, M.; Fiumelli, H.; Magistretti, P. J.; McCulloch, I.; et al. Photo-Chemical Stimulation of Neurons with Organic Semiconductors. *Adv. Sci.* **2023**, *10* (31), No. 2300473.
(33) Tavakkolnia, I.; Jagadamma, L. K.; Bian, R.; Manousiadis, P. P.; Videv, S.; Turnbull, G. A.; Samuel, I. D. W.; Haas, H. Organic photovoltaics for simultaneous energy harvesting and high-speed MIMO optical wireless communications. *Light: Sci. Appl.* **2021**, *10* (1), No. 41.
(34) Dang, M. T.; Hirsch, L.; Wantz, G. P3HT:PCBM, Best Seller in Polymer Photovoltaic Research. *Adv. Mater.* **2011**, *23* (31), 3597−3602.
(35) Schulz, M.; Balzer, F.; Scheunemann, D.; Arteaga, O.; Lützen, A.; Meskers, S. C. J.; Schiek, M. Chiral Excitonic Organic Photodiodes for Direct Detection of Circular Polarized Light. *Adv. Funct. Mater.* **2019**, *29* (16), No. 1900684.
(36) Zhu, L.; Zhang, M.; Zhou, Z.; Zhong, W.; Hao, T.; Xu, S.; Zeng, R.; Zhuang, J.; Xue, X.; Jing, H.; et al. Progress of organic photovoltaics towards 20% efficiency. *Nat. Rev. Electr. Eng.* **2024**, *1* (9), 581−596.
(37) Park, S. Y.; Chandrabose, S.; Price, M. B.; Ryu, H. S.; Lee, T. H.; Shin, Y. S.; Wu, Z.; Lee, W.; Chen, K.; Dai, S.; et al. Photophysical pathways in efficient bilayer organic solar cells: The importance of interlayer energy transfer. *Nano Energy* **2021**, *84*, No. 105924.
(38) Karatum, O.; Yildiz, E.; Kaleli, H. N.; Sahin, A.; Ulgut, B.; Nizamoglu, S. RuO2 Supercapacitor Enables Flexible, Safe, and Efficient Optoelectronic Neural Interface. *Adv. Funct. Mater.* **2022**, *32* (31), No. 2109365.
(39) Park, Y.; Chung, T. S.; Lee, G.; Rogers, J. A. Materials Chemistry of Neural Interface Technologies and Recent Advances in Three-Dimensional Systems. *Chem. Rev.* **2022**, *122* (5), 5277−5316.
(40) Han, M.; Srivastava, S. B.; Yildiz, E.; Melikov, R.; Surme, S.; Dogru-Yuksel, I. B.; Kavakli, I. H.; Sahin, A.; Nizamoglu, S. Organic Photovoltaic Pseudocapacitors for Neurostimulation. *ACS Appl. Mater. Interfaces* **2020**, *12* (38), 42997−43008.
(41) Terutsuki, D.; Yoroizuka, H.; Osawa, S.-i.; Ogihara, Y.; Abe, H.; Nakagawa, A.; Iwasaki, M.; Nishizawa, M. Totally Organic Hydrogel-Based Self-Closing Cuff Electrode for Vagus Nerve Stimulation. *Adv. Healthcare Mater.* **2022**, *11* (23), No. 2201627.
(42) Ejneby, M. S.; Migliaccio, L.; Gicevičius, M.; Đerek, V.; Jakešová, M.; Elinder, F.; Głowacki, E. D. Extracellular Photovoltage Clamp Using Conducting Polymer-Modified Organic Photocapacitors. *Adv. Mater. Technol.* **2020**, *5* (3), No. 1900860.
(43) Yuk, H.; Lu, B.; Zhao, X. Hydrogel bioelectronics. *Chem. Soc. Rev.* **2019**, *48* (6), 1642−1667.
(44) Zhao, W.; Qian, D.; Zhang, S.; Li, S.; Inganäs, O.; Gao, F.; Hou, J. Fullerene-Free Polymer Solar Cells with over 11% Efficiency and Excellent Thermal Stability. *Adv. Mater.* **2016**, *28* (23), 4734−4739.
(45) Sheberla, D.; Bachman, J. C.; Elias, J. S.; Sun, C.-J.; Shao-Horn, Y.; Dincă, M. Conductive MOF electrodes for stable supercapacitors with high areal capacitance. *Nat. Mater.* **2017**, *16* (2), 220−224.
(46) Prominski, A.; Shi, J.; Li, P.; Yue, J.; Lin, Y.; Park, J.; Tian, B.; Rotenberg, M. Y. Porosity-based heterojunctions enable leadless optoelectronic modulation of tissues. *Nat. Mater.* **2022**, *21* (6), 647−655.
(47) Abdullaeva, O. S.; Balzer, F.; Schulz, M.; Parisi, J.; Lützen, A.; Dedek, K.; Schiek, M. Organic Photovoltaic Sensors for Photo-

capacitive Stimulation of Voltage-Gated Ion Channels in Neuroblastoma Cells. *Adv. Funct. Mater.* **2019**, *29* (21), No. 1805177.
(48) Han, M.; Karatum, O.; Nizamoglu, S. Optoelectronic Neural Interfaces Based on Quantum Dots. *ACS Appl. Mater. Interfaces* **2022**, *14* (18), 20468−20490.
(49) Du, X.; Heumueller, T.; Gruber, W.; Classen, A.; Unruh, T.; Li, N.; Brabec, C. J. Efficient Polymer Solar Cells Based on Non-fullerene Acceptors with Potential Device Lifetime Approaching 10 Years. *Joule* **2019**, *3* (1), 215−226.
(50) Nguyen, D. K.; Schepisi, I. M.; Amir, F. Z. Extraordinary cycling stability of $Ni_3(HITP)_2$ supercapacitors fabricated by electrophoretic deposition: Cycling at 100,000 cycles. *Chem. Eng. J.* **2019**, *378*, No. 122150.
(51) Langer, R.; Tirrell, D. A. Designing materials for biology and medicine. *Nature* **2004**, *428* (6982), 487−492.
(52) Cai, D.; Lu, M.; Li, L.; Cao, J.; Chen, D.; Tu, H.; Li, J.; Han, W. A Highly Conductive MOF of Graphene Analogue Ni3(HITP)2 as a Sulfur Host for High-Performance Lithium−Sulfur Batteries. *Small* **2019**, *15* (44), No. 1902605.
(53) Jiang, Y.; Carvalho-de-Souza, J. L.; Wong, R. C. S.; Luo, Z.; Isheim, D.; Zuo, X.; Nicholls, A. W.; Jung, I. W.; Yue, J.; Liu, D.-J.; et al. Heterogeneous silicon mesostructures for lipid-supported bioelectric interfaces. *Nat. Mater.* **2016**, *15* (9), 1023−1030.
(54) Wu, G.; Huang, J.; Zang, Y.; He, J.; Xu, G. Porous Field-Effect Transistors Based on a Semiconductive Metal−Organic Framework. *J. Am. Chem. Soc.* **2017**, *139* (4), 1360−1363.
(55) Dykstra, S.; Turner, R. W. Rebound Depolarizations. In *Essentials of Cerebellum and Cerebellar Disorders*; Gruol, D. L.; Koibuchi, N.; Manto, M.; Molinari, M.; Schmahmann, J. D.; Shen, Y., Eds.; Springer: Cham, 2023.
(56) Aizenman, C. D.; Linden, D. J. Regulation of the rebound depolarization and spontaneous firing patterns of deep nuclear neurons in slices of rat cerebellum. *J. Neurophysiol.* **1999**, *82* (100), 1697−1709.
(57) Liu, Q.; Bottle, S. E.; Sonar, P. Developments of Diketopyrrolopyrrole-Dye-Based Organic Semiconductors for a Wide Range of Applications in Electronics. *Adv. Mater.* **2020**, *32*, No. 1903882.
(58) Lei, Y.; Deng, P.; Lin, M.; Zheng, X.; Zhu, F.; Ong, B. S. Enhancing Crystalline Structural Orders of Polymer Semiconductors for Efficient Charge Transport via Polymer-Matrix-Mediated Molecular Self-Assembly. *Adv. Mater.* **2016**, *28*, 6687−6694.
(59) Surya, S. G.; Nagarkar, S. S.; Ghosh, S. K.; Sonar, P.; Rao, V. R. OFET based explosive sensors using diketopyrrolopyrrole and metal organic framework composite active channel material. *Sens. Actuators, B* **2016**, *223*, 114−122.
(60) Kandel, E.; Schwartz, J.; Jessell, T.; Siegelbaum, S.; Hudspeth, A. J. *Principles of Neural Science*, 5; McGraw Hill: 2013.

https://doi.org/10.1021/acsnano.5c01516
ACS Nano 2025, 19, 16813−16828

Supporting Information

Metal-Organic Frameworks Modified Organic Bulk Heterojunction Interfaces for Effective Nongenetic Neuromodulation

Kangkang Weng,[†,§⊥] Wenjun Li,[†⊥] Xinyu Cheng,[†⊥] Yunyun Xing,[‡⊥] Xin Fu,[#] Yinghan Wang,[‡] Huachun Wang,[#] Xiaoli Tian,[†] Yuqi Wang,[#] Lizhu Li,[#,ϕ] Jun Yao,[‡] Xing Sheng,[#*] Jinghong Li,[†*] Hao Zhang[†*]*

† Department of Chemistry, Center for Bioanalytical Chemistry, Key Laboratory of Bioorganic Phosphorus Chemistry & Chemical Biology (Ministry of Education), Tsinghua University, Beijing 100084, China

§ School of Optics and Photonics, Beijing Key Laboratory for Precision Optoelectronic Measurement Instrument and Technology, Beijing Institute of Technology, Beijing 100081, China

‡ School of Life Sciences, State Key Laboratory of Membrane Biology, Tsinghua-Peking Center for Life Sciences, IDG/McGovern Institute for Brain Research, Tsinghua University, Beijing 100084, China

Department of Electronic Engineering, Beijing National Research Center for Information Science and Technology, Institute for Precision Medicine, Laboratory of Flexible Electronics Technology, IDG/McGovern Institute for Brain Research, Tsinghua University, Beijing 100084, China

♮ Sichuan Provincial Key Laboratory for Human Disease Gene Study and the Center for Medical Genetics, School of Life Science and Technology, University of Electronic Science and Technology of China, Chengdu, 611731, China

*Email: jyao@mail.tsinghua.edu.cn; xingsheng@mail.tsinghua.edu.cn; jhli@mail.tsinghua.edu.cn; hzhangchem@mail.tsinghua.edu.cn

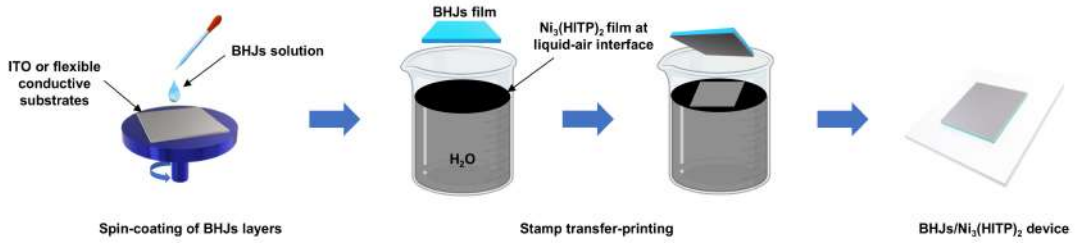

Figure S1. Schematic illustration of fabrication procedures of the BHJs/$Ni_3(HITP)_2$ devices.

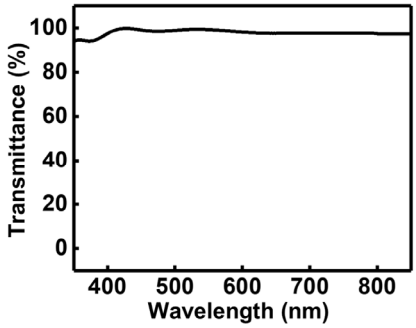

Figure S2. The optical transmission spectrum of $Ni_3(HITP)_2$ film.

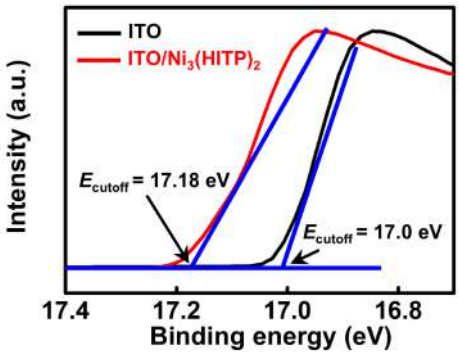

Figure S3. **UPS spectra of $Ni_3(HITP)_2$.** The Fermi energy level (E_F) was obtained directly from the UPS data and calculated by the following equation, $E_F = h\nu - E_{cutoff}$.

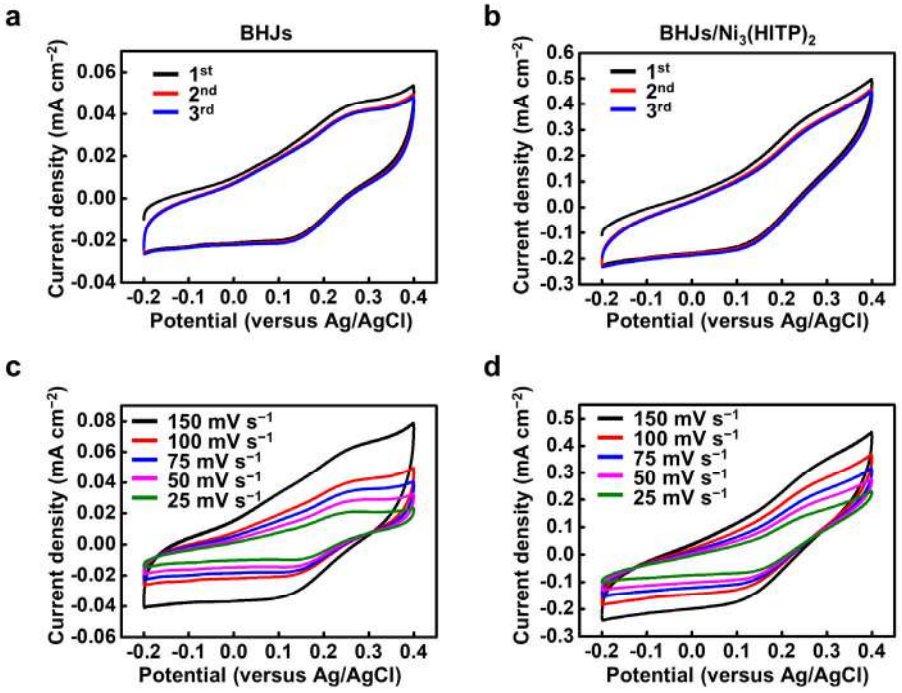

Figure S4. Cyclic voltammetry of BHJ-only and BHJs/$Ni_3(HITP)_2$ devices in PBS solution. (a,b) The first 3 scans at the sweep speed of 100 mV s^{-1}. **(c,d)** Data collected at different sweep speeds (25, 50, 75, 100, 150 mV s^{-1}). Data from the 2nd scan at various sweep speeds were used for making panels c,d. At all sweep speeds, the integrated area of data from BHJs/$Ni_3(HITP)_2$ devices was 5 times of that from BHJs-only devices.

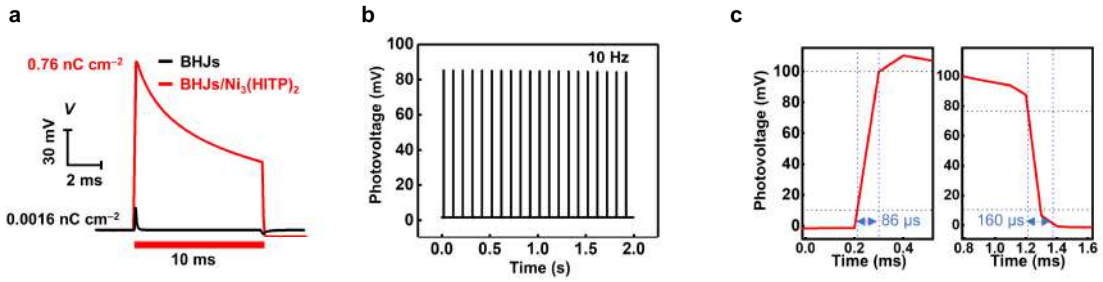

Figure S5. Additional photo-induced voltage data of BHJs-only and BHJs/$Ni_3(HITP)_2$ devices. (a) Photovoltage of BHJs-only and BHJs/$Ni_3(HITP)_2$ devices under laser illumination (indicated by the red bar). Illumination condition, 635 nm, spot size ≈4 mm; pulse duration, 10 ms; light intensity, 20 mW mm^{-2}. **(b)** Photovoltage recorded from BHJs/$Ni_3(HITP)_2$ devices under laser illumination at 10 Hz for 2 s. **(c)** Photovoltage of BHJs/$Ni_3(HITP)_2$ devices show rapid rise (≈86 μs) and decay (≈160 μs) after laser illumination (635 nm, spot size ≈4 mm; pulse duration, 5 ms; light intensity, 20 mW mm^{-2}).

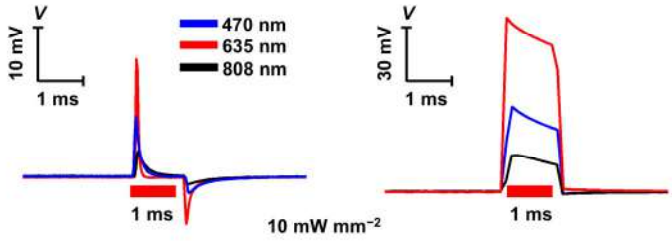

Figure S6. Photovoltage traces recorded from PBDB-T:ITIC and PBDB-T:ITIC/$Ni_3(HITP)_2$ devices under the irradiation of lasers with wavelengths of 470, 635, and 808 nm. Laser intensity, 10 mW mm^{-2}; pulse width, 1 ms; spot size, 4 mm.

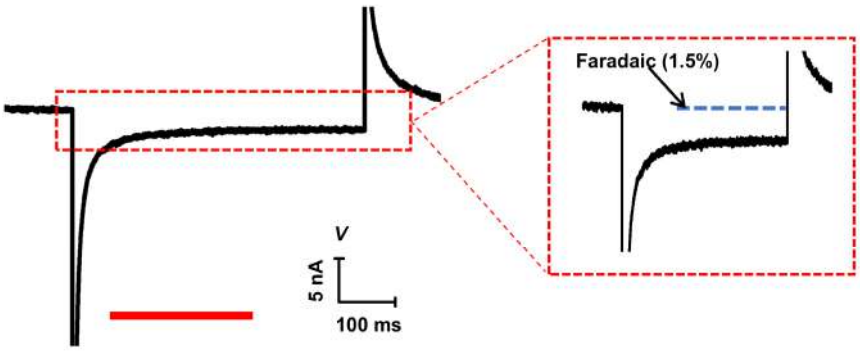

Figure S7. Photocurrent curve of the BHJs/$Ni_3(HITP)_2$ devices under 635 nm illumination. The magnified view on the right indicates that the photocurrent is mostly capacitive with minimal faradaic component (<1.5%). Pulse width, 500 ms; light intensity, 15 mW mm^{-2}; spot size, ≈4 mm.

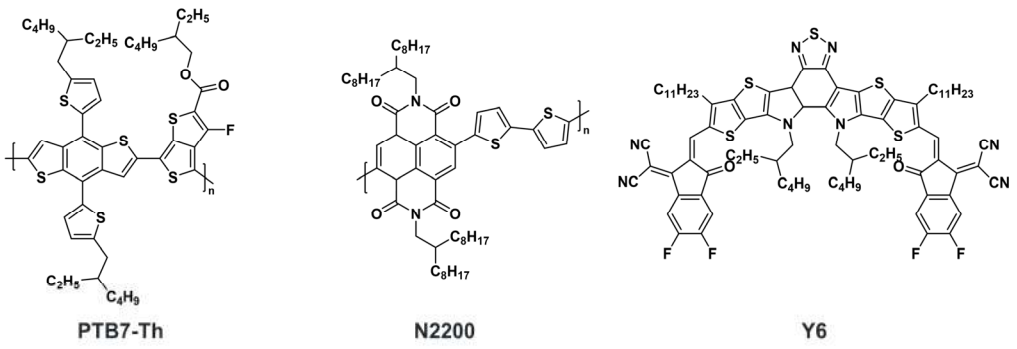

Figure S8. Molecular structures of other donors and acceptors for BHJs used in this work. PTB7-Th is a donor. N2200 is a polymeric acceptor and Y6 is a near-infrared acceptor.

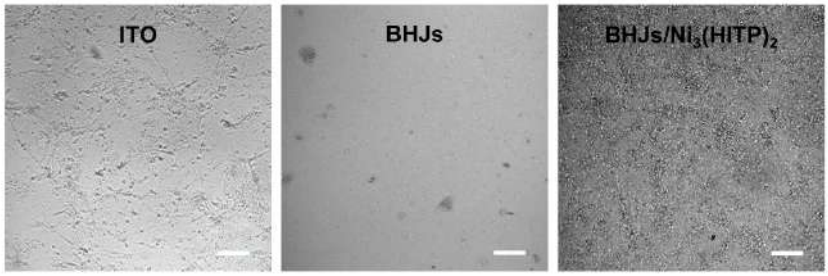

Figure S9. Optical microscopic images of mouse primary hippocampal neurons cultured on different substrates. The images were obtained on day 7 to observe the cell distribution on ITO (control), BHJs, and BHJs/ $Ni_3(HITP)_2$ substrates, respectively. Scale bars, 100 μm.

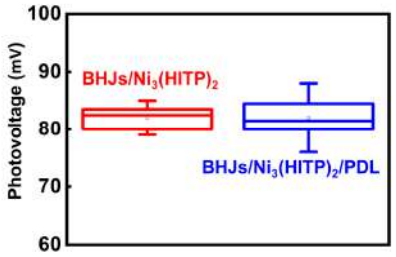

Figure S10. Comparison of the photovoltage of BHJs/$Ni_3(HITP)_2$ devices before and after PDL coating. Illumination used a 635 nm laser, spot size, ≈4 mm; pulse width,10 ms; intensity, 20 mW mm^{-2}. A total of five measurements (n = 5) were conducted on the devices. Box plots show the interquartile range (IQR) centered around the median, with whiskers extending to 1.5 times the IQR above and below the box.

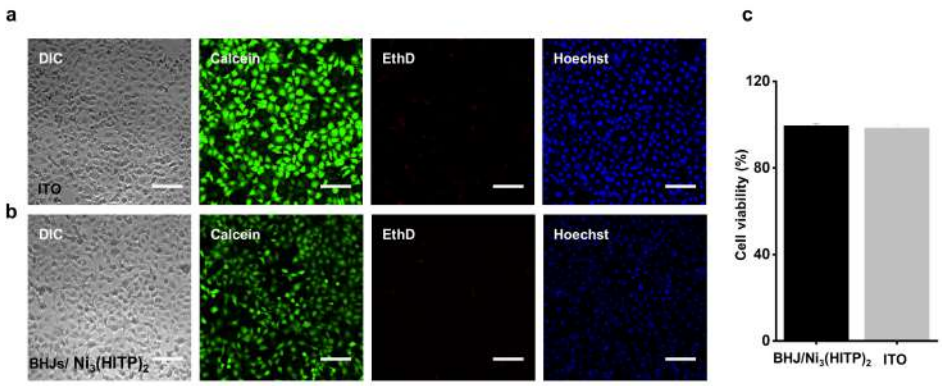

Figure S11. Cell biocompatibility of MCF7 cells cultured on BHJs/$Ni_3(HITP)_2$ devices. **(a)** Live/dead assay of MCF7 cells incubated on ITO and **(b)** BHJs/$Ni_3(HITP)_2$ devices. The images with blue (Hoechst), green (Calcien AM), and red (Ethidium homodimer-1, EthD-1) color represent cell nuclei, live cells, and dead cells, respectively. Scale bars, 100 μm. **(c)** Biocompatibility measured by CCK-8 assay of MCF7 cells incubated on ITO and of BHJs/$Ni_3(HITP)_2$ devices, respectively.

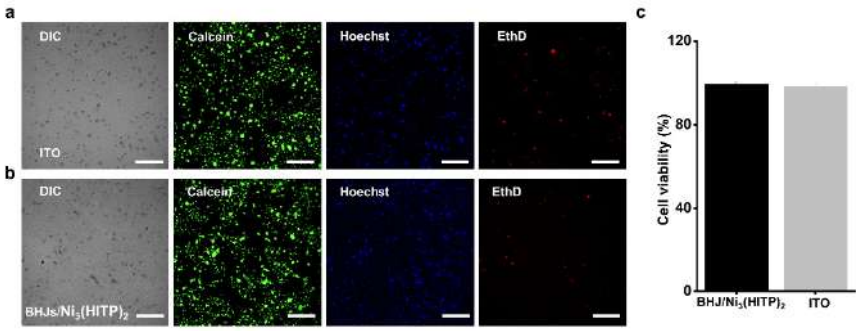

Figure S12. Cell biocompatibility of rat DRG cells cultured on BHJs/$Ni_3(HITP)_2$ devices. (a) Live/dead assay of DRG cells incubated on ITO and **(b)** BHJs/$Ni_3(HITP)_2$ devices. The images with blue (Hoechst), green (Calcien AM), and red (Ethidium homodimer-1, EthD-1) color represent cell nuclei, live cells and dead cells respectively. Scale bars, 100 μm. **(c)** Biocompatibility measured by CCK-8 assay of rat DRG cells incubated on ITO and of BHJs/$Ni_3(HITP)_2$ devices, respectively.

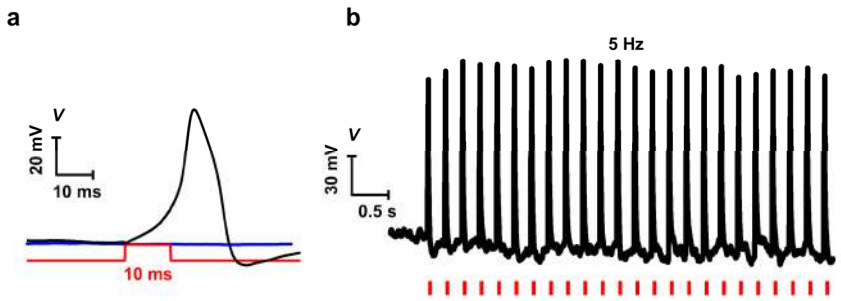

Figure S13. Additional data of the photostimulation of rat DRG neurons by BHJs/$Ni_3(HITP)_2$ devices under pulsed illumination. (a) Membrane potential traces of cultured rat DRG neurons photostimulated by BHJs/$Ni_3(HITP)_2$ device (black) and ITO (blue, as control), respectively. The red bars indicate the laser pulses (10 ms). **(b)** Reproducible firing of cultural DRG neurons on BHJs/$Ni_3(HITP)_2$ at the frequency of 5 Hz. The red bars indicate the laser pulses. Parameters for laser illumination, 635 nm, spot size, ≈500 μm; light intensity, 750 mW mm^{-2}; pulse width, 10 ms.

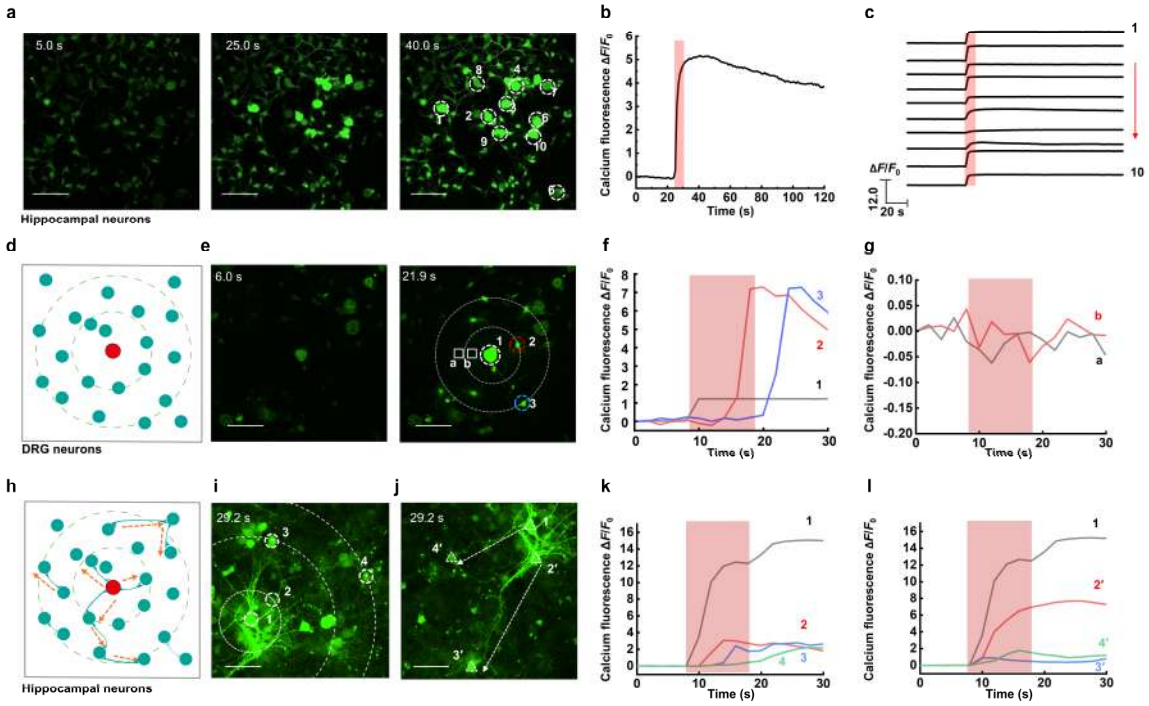

Figure S14. Calcium imaging of cultured neurons optically modulated by BHJs/$Ni_3(HITP)_2$ devices. (a) Calcium imaging of mouse primary hippocampal neurons cultured on BHJs/$Ni_3(HITP)_2$ devices before light exposure (e.g., 5.0 s), during light irradiation (25.0 s), and after the termination of irradiation (e.g., 40.0 s). In the case, all neurons in the field of view were irradiated and excited. Ten neurons (white dashed circles) were randomly selected as regions of interest (ROIs) for fluorescence analysis. **(b,c)** Normalized $\Delta F/F_0$ of mouse primary hippocampal neuron #1 (panel b) and all 10 neurons (panel c) marked in panel a, recorded over time. Red bars indicate the duration of laser illumination. **(d)** Schematic diagram of calcium wave propagation pathway (indicated by the green dashed circles) in rat DRG neurons during single-cell photostimulation. The red dot represents the single, irradiated neuron, and the green dots represent neighboring, non-irradiated neurons. **(e)** Calcium imaging of rat DRG neurons before irradiation (e.g., 6.0 s) and right after the termination of light irradiation (e.g., 21.9 s). Neuron #1 (white dashed

circle) was irradiated, while its neighbors (neurons #2 and #3, in the red and blue dashed circles, respective) were not. **(f)** Normalized $\Delta F/F_0$ changes of neurons #1, #2, and #3 from panel e, recorded before, during, and after neuron #1 was irradiated. Red bar indicates laser illumination duration. Neuron #1, the single-cell under irradiation, was excited first, followed by neurons #2 and then #3. The onset time sequence of excitation in neurons #2 and #3 correlates with their distance to neuron #1, suggesting the calcium wave propagation pathway triggered by the firing event of neuron #1. **(g)** Normalized $\Delta F/F_0$ changes of neuron #1, when irradiated regions (denoted by the white squares "a" and "b") contained no neurons. No changes in normalized $\Delta F/F_0$ were observed. **(h)** Schematic of two potential pathways, namely the calcium wave propagation (indicated by the green dashed circles) and neural network transmission via synaptic connections (indicated by the red dashed arrows) in mouse primary hippocampal neurons during single-cell photostimulation. The red dot represents the single neuron under irradiation and the green dots represent neighboring neurons. **(i–l)** Calcium imaging of mouse primary hippocampal neurons cultured on BHJs/$Ni_3(HITP)_2$ (panels i,j). In panel i, neuron #1 was irradiated, while neurons #2–#4 were not. Changes in normalized $\Delta F/F_0$ for these non-irradiated neurons (panel k) indicate that calcium wave propagation was the dominant pathway, because the onset time sequence aligns with the distance of these neurons from neuron #1. In panel j, neuron #1 (the same with neuron #1 in panel i) induced excitation of non-irradiated neurons (#2'–#4', as shown by recorded changes in normalized $\Delta F/F_0$ in panel l), possibly through synaptic transmission, as excitation time sequence of normalized $\Delta F/F_0$ changes does not fully correlate with their distance from neuron #1. Data in panels (a–c) were collected during the photostimulation of all neurons in the field of view with an external 635 nm

laser (power density, 10 mW mm^{-2}; frequency, 5 Hz; pulses width, 1 ms). Data in panels (d–l) were collected during the photostimulation of neurons with a built-in 635 nm laser in the microscope (0.22 mW) to achieve single-cell precision. Scale bars, (a) 100 μm, (e, i, j) 50 μm.

We conducted dynamic calcium (Ca^{2+}) imaging of 10 mouse primary hippocampal neurons cultured on BHJs/Ni_3(HITP)$_2$ (neurons #1–#10 marked by white dashed circles in Figure S14a). In this case, all neurons in the field of view were irradiated and modulated by an external 635 nm laser. The neurons were stained with Calbryte-520 AM Ca^{2+} indicators to monitor fluorescence changes. Upon illumination (10 mW mm^{-2}; spot size, ≈4 mm; pulse frequency, 5 Hz; pulse duration, 1 ms), all neurons show significant increase in Ca^{2+} fluorescence intensity, with $\Delta F/F$ rising about fivefold (Figure S14b,c). In comparison, mouse primary hippocampal neurons cultured on ITO glass substrates (Figure S14) or glass/BHJs/Ni_3(HITP)$_2$ (Figure S15) show minimal fluorescent changes ($\Delta F/F$ <10%) under identical irradiated conditions. This comparison confirms the photocapacitive origin of the neuromodulation.

We can also selectively stimulate a single neuron and monitor the Ca^{2+} fluorescence changes of both the targeted neuron and its neighbor cells. To achieve the single-cell resolution, we used a built-in 635 nm laser in the microscope as the irradiation source. This approach enables us to investigate intercellular communication for different types of neurons, such as rat DRG and mouse primary hippocampal neurons. For instance, DRG neurons extracted from adult rats lack synaptic connections between the neurons (Figure

S14d). Consequently, selective excitation of a single DRG neuron (cell #1, as marked by the white dashed circle in Figure S14e) results in localized ramp in Ca^{2+} signals (reflected by normalized $\Delta F/F$), which gradually diminishes after the illumination (Figure S14f). Although not directly irradiated, neighboring glial cells (e.g., cells #2 and #3) show upregulated Ca^{2+} dynamics with a relatively long delay (≈5–10 s after the excitation of neuron #1), which were probably triggered by the firing event of cell #1 through a slow Ca^{2+} wave propagation pathway (illustrated by the green sphere in Figure S14d).[1] This proposed Ca^{2+} wave propagation mechanism also explains the observed correlation between the excitation onset time for cells #2 and #3 and their respective distances from cell #1. To exclude the possibility of random neuron firing, we directed the laser beam at cell-free regions (e.g., spots #a and #b in the white squares) and recorded no changes in the fluorescence of neuron #1 (Figure S14g).

Unlike rat DRG neurons, mouse primary hippocampal neurons have abundant synaptic connections, which provide additional pathways for intercellular communication (Figure S14h). Similar to the modulation of DRG neurons, we selectively targeted and excited a single neuron (denoted as #1 in Figure S14i,j). The fluorescence intensity changes of neighboring neurons (data in panel k correspond to #2, #3, #4 in Figure S14i, and data in panel l correspond to #2′, #3′, #4′ in Figure S14j) show different patterns. As shown in Figure S14k, the onsets of increased Ca^{2+} fluorescence intensities followed a sequence of neurons #2 (9.9 s), #3 (13.9 s), and #4 (15.9 s), consistent with their distance to neuron #1. This sequential pattern resembles that observed in rat DRG neurons and can be ascribed to the Ca^{2+} wave propagation. Meanwhile, the same neuron #1 also induces changes in the

fluorescence intensities of another group of neighboring neurons (#2′, #3′, #4′), but with faster response times (onset time ≈7.9 s, Figure S14l). Notably, neuron #3′, which is farther away from #1, exhibits a similar onset time to neuron #4′. The fast response time and weak correlation with distance suggest that these signals are transmitted through synaptic connections within the neural networks rather than Ca^{2+} waves. The ability to identify signal propagation pathways in different types of neurons renders these devices promising in unravelling more functional features of neural networks and their associated structural circuitry, when incorporated with imaging techniques.

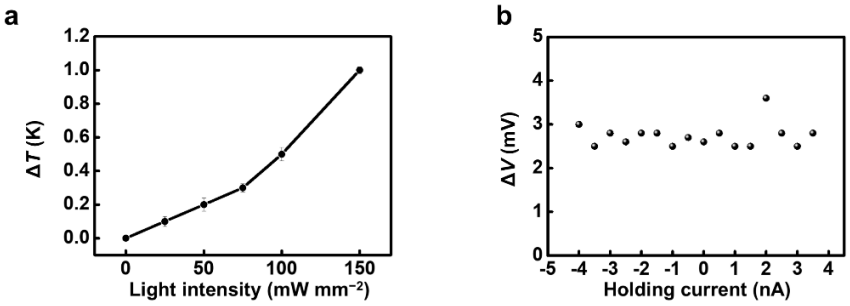

Figure S15. Evaluation of the photothermal effect in the bidirectional neuromodulation by BHJs/$Ni_3(HITP)_2$ devices. (a) Temperature increases near the surface of BHJs/$Ni_3(HITP)_2$ devices (immersed in PBS) during low-intensity, continuous (5 s) illumination (635 nm, spot size, ≈500 μm). The temperature was measured by a probe placed near the device surface. **(b)** Evaluation of the photothermal effect of BHJs/$Ni_3(HITP)_2$ devices under intense and pulsed illumination (635 nm, spot size, ≈500 μm; 750 mW mm^{-2}; pulse width, 10 ms). Holding current dependent photovoltage. $\Delta V_{light,10\ ms}$ versus I_0 exhibits a minimal slope, indicating that the BHJs/$Ni_3(HITP)_2$ device has a weak photothermal response. In both (a) and (b), the estimated temperature increase was less than 1 °C, regardless of irradiation duration (5 s or a pulse width of 10 ms). In cellular experiments, the intensity of continuous light was typically less than 150 mW mm^{-2}.

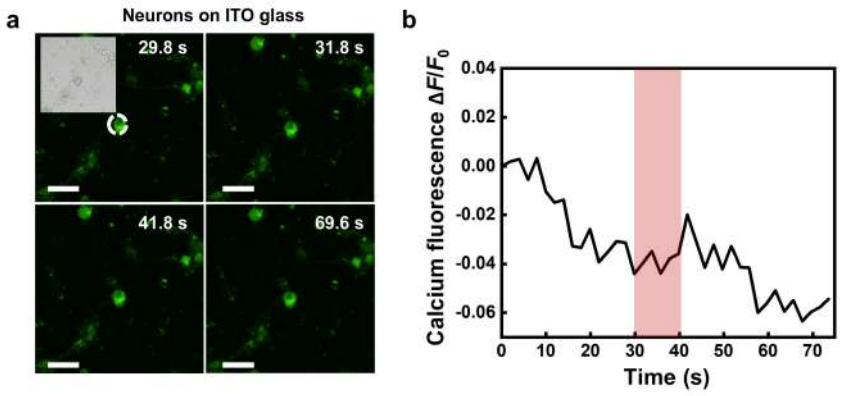

Figure S16. Calcium dynamics for mouse primary hippocampal neurons cultured on ITO glass under illumination, as a control group. (a) Fluorescence images of neurons labeled with Calbryte-520 AM on ITO taken before (29.8 and 31.8 s), during (41.8 s), and after (69.6 s) illumination. The laser, set at 2 mW, was focused on the target neuron (indicated by the white-marked region). Inset in (a) shows a bright field image of the cultured neurons. **(b)** Normalized $\Delta F/F_0$ over time of the neurons marked by the white dashed circle in (a). The red area denotes laser illumination time (about 10 s). The changes in $\Delta F/F_0$ is negligible. Scale bars, 50 μm.

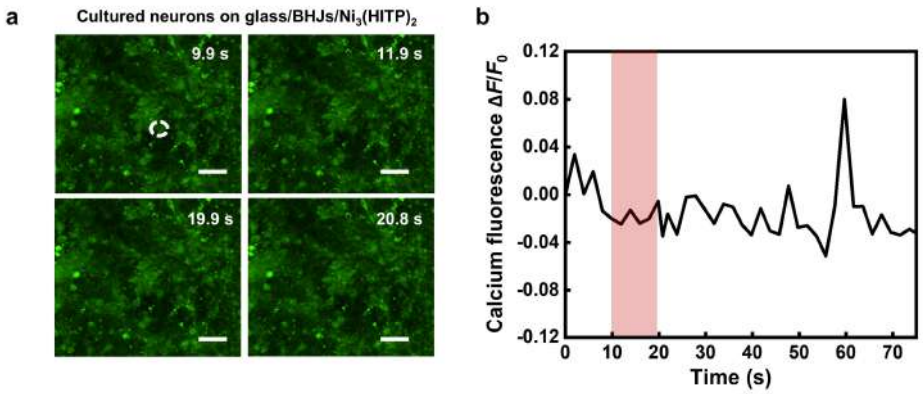

Figure S17. Calcium dynamics for mouse primary hippocampal neurons cultured on glass/BHJs/$Ni_3(HITP)_2$ under illumination, as a control group. (a) Fluorescence images of neurons labeled with Calbryte-520 AM on ITO taken before (9.9 s), during (11.9, 19.9 s), and after (20.8 s) illumination. The laser, set at 2 mW, was focused on the target neuron (indicated by the white-marked region). **(b)** Normalized $\Delta F/F_0$ over time of the neurons marked by the white dashed circle in (a). The red area denotes laser illumination time (about 10 s). The changes in $\Delta F/F_0$ is negligible. Scale bars, 50 μm.

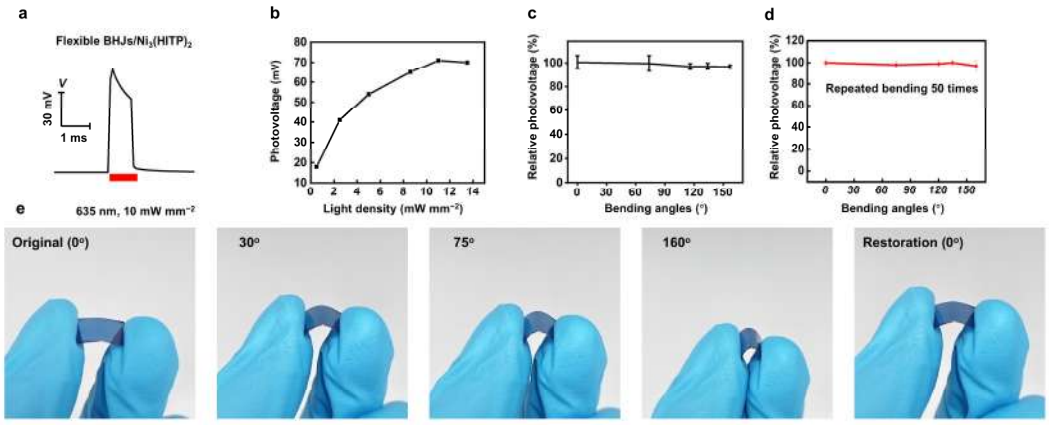

Figure S18. Photoresponses of BHJs/$Ni_3(HITP)_2$ devices made on flexible substrates during bending cycles. (a) Recorded photoresponse of the flexible devices on polyimide substrates under 635 nm laser illumination (spot size, ≈4 mm; light intensity, 10 mW mm^{-2}). The red bar indicates the illumination duration (1 ms). **(b)** The dependance of photovoltage on light intensities for flexible devices on polyimide substrates. **(c,d)** Photovoltage of flexible devices on polyethylene terephthalate substrates remains unaffected with bending angles up to 160° and during multiple (50 times) bending cycles at various bending angles. **(e)** Photographs of devices at various bending angles and after returning to its initial state.

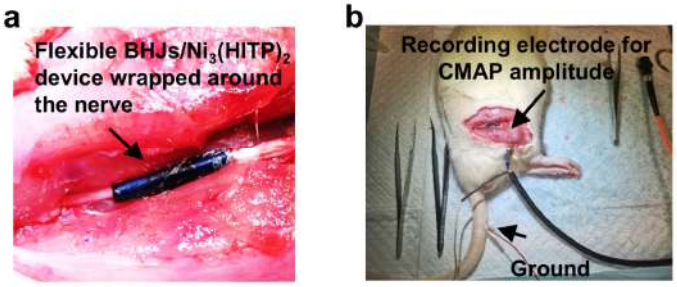

Figure S19. Photographs of the setup for *in vivo* photostimulation of the sciatic nerve of anesthetized rats. Flexible BHJs-only and BHJs/$Ni_3(HITP)_2$ devices were wrapped around the exposed sciatic nerve of rats and a recording electrode was placed nearby to collect the CMAP amplitude.

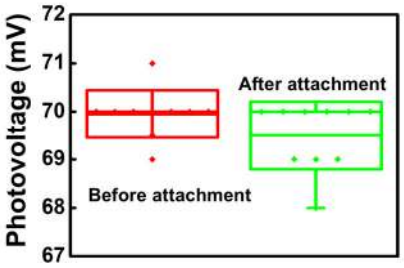

Figure S20. Photovoltage of BHJ/$Ni_3(HITP)_2$ devices before and after the *in vivo* rat sciatic nerve modulation experiment.

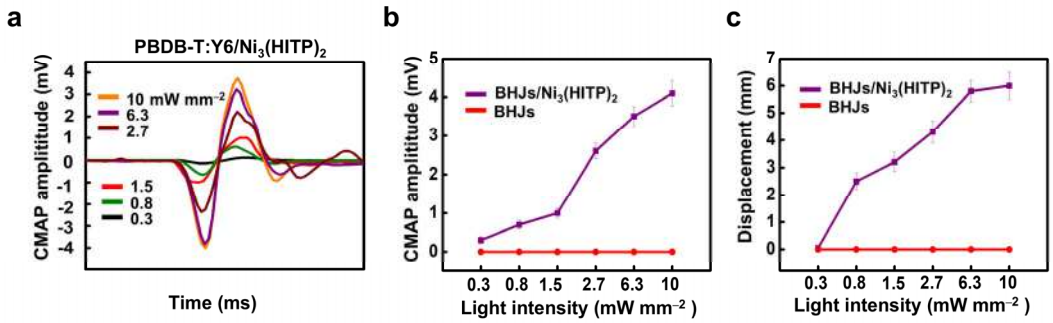

Figure S21. ***In vivo*** **peripheral neuromodulation using PBDB-T:Y6/$Ni_3(HITP)_2$ devices on rat models under 808-nm near infrared light. (a)** Typical CMAPs evoked by illuminating the BHJs-only or BHJs/$Ni_3(HITP)_2$ devices on one hindlimb of rat with various light intensities. 808 nm, Light pulse duration, 1 ms; frequency, 1 Hz. (b,c) Statistics of recorded **(b)** CMAP amplitudes near the sciatic nerve and **(c)** limb displacements of rats implanted with BHJs-only and BHJ/$Ni_3(HITP)_2$ devices, respectively, under various light intensities (pulse duration, 1 ms; frequency,1 Hz).

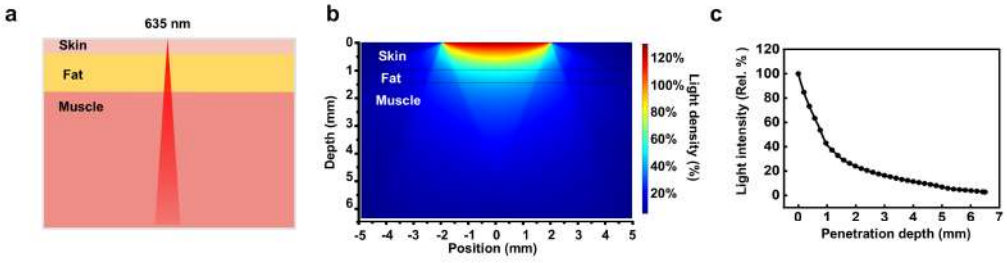

Figure S22. Simulation light intensity decay along the depths of rat skin and tissue. **(a)** A scheme of the penetration of 635 nm light along the skin, fat and muscle layers of rat. **(b)** Numerical simulation of the spatial distribution and intensity decay of a 635 nm red light (125 mW mm^{-2}) beam under rat skin. **(c)** Simulated attenuation of 635 nm light at various depths. Based on the data in panel (c), to obtain 1 mW mm^{-2} at a depth of 6 mm, which is sufficient to trigger CAMPs according to Fig. 6e,f, the required light intensity exposed to skin was calculated to be 38 mW mm^{-2}. Such low-intensity pulses (pulse width, 1 ms) correlate to an energy density of 0.04 mJ cm^{-2}, which is 3–4 orders of magnitude lower than the accepted laser safety standards for skin exposure (e.g., the American National Safety Standard for the use of lasers, 195 mJ cm^{-2})[2].

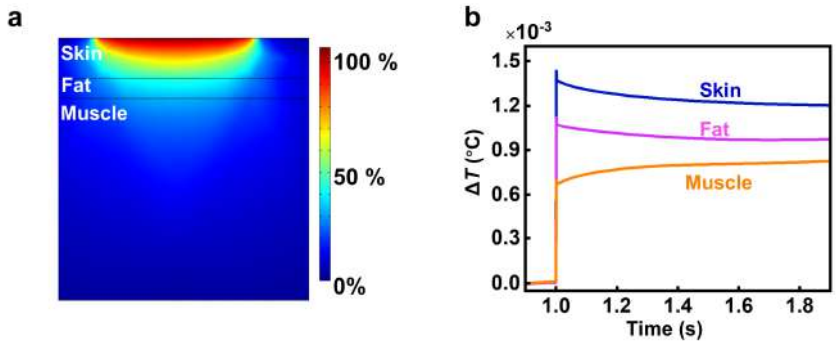

Figure S23. Simulated temperature increases in animal tissues during photostimulation. (a) Simulated temperature profile in rat skin, fat and muscle. **(b)** Simulated temperature increases during the laser illumination. The illumination parameters for the simulation included, wavelength 635 nm; spot size, 4 mm; light intensity, 700 mW cm^{-2}; pulse duration, 1 ms. The temperature increases were far below 1 °C.

Movie S1. Ca^{2+} imaging during photostimulation of cultured mouse hippocampal neurons and rat DRG neurons by BHJs/$Ni_3(HITP)_2$ devices.

Movie S2. Recorded rat hindlimb movement during the photostimulation of sciatic nerve by BHJs/$Ni_3(HITP)_2$ devices.

References

(1) W. N. Ross, Understanding calcium waves and sparks in central neurons. *Nat. Rev. Neurosci.* **2012**, *13* (3), 157-168.

(2) A. N. Bashkatov, E. A. Genina, V. V. Tuchin, OPTICAL PROPERTIES OF SKIN, SUBCUTANEOUS, AND MUSCLE TISSUES: A REVIEW. *J. Innov. Opt. Health Sci.* **2011**, *04* (1), 9-38.